Title

3D modeling of deep borehole electromagnetic measurements with energized casing source for fracture mapping at the Utah Frontier Observatory for Research in Geothermal Energy

Journal

Geophysical Prospecting, 72(8)

ISSN

0016-8025

Authors

Um, Evan Schankee

Alumbaugh, David

Capriotti, Joseph

et al.

Publication Date

2024-10-01

DOI

10.1111/1365-2478.13579

Peer reviewed

Received: 16 May 2023 | Accepted: 15 July 2024

DOI: 10.1111/1365-2478.13579

Geophysical Prospecting | EAGE EUROPEAN ASSOCIATION OF GEOSCIENTISTS & ENGINEERS

ORIGINAL ARTICLE

3D modeling of deep borehole electromagnetic measurements with energized casing source for fracture mapping at the Utah Frontier Observatory for Research in Geothermal Energy

Evan Schankee Um[1] | **David Alumbaugh**[1] | **Joseph Capriotti**[2] | **Michael Wilt**[1] | **Edward Nichols**[1] | **Yaoguo Li**[2] | **Seogi Kang**[3] | **Kazumi Osato**[4]

[1]Earth and Environmental Sciences, Lawrence Berkeley National Laboratory, Berkeley, California, USA

[2]Department of Geophysics, Colorado School of Mines, Golden, Colorado, USA

[3]Department of Geophysics, Stanford University, Stanford, California, USA

[4]Geothermal Energy Research and Development Co. Ltd, Tokyo, Japan

Correspondence
Evan Schankee Um, Earth and Environmental Sciences, Lawrence Berkeley National Laboratory, Berkeley, CA, USA.
Email: esum@lbl.gov

Funding information
The U.S. DOE EERE Geothermal Technologies Office, Utah FORGE and the University of Utah

Abstract

We present a 3D numerical modelling analysis evaluating the deployment of a borehole electromagnetic measurement tool to detect and image a stimulated zone at the Utah Frontier Observatory for Research in Geothermal Energy geothermal site. As the depth to the geothermal reservoir is several kilometres and the size of the stimulated zone is limited to several 100 m, surface-based controlled-source electromagnetic measurements lack the sensitivity for detecting changes in electrical resistivity caused by the stimulation. To overcome the limitation, the study evaluates the feasibility of using a three-component borehole magnetic receiver system at the Frontier Observatory for Research in Geothermal Energy site. To provide sufficient currents inside and around the enhanced geothermal reservoir, we use an injection well as an energized casing source. To efficiently simulate energizing the injection well in a realistic 3D resistivity model, we introduce a novel modelling workflow that leverages the strengths of both 3D cylindrical-mesh-based electromagnetic modelling code and 3D tetrahedral-mesh-based electromagnetic modelling code. The former is particularly well-suited for modelling hollow cylindrical objects like casings, whereas the latter excels at representing more complex 3D geological structures. In this workflow, our initial step involves computing current densities along a vertical steel-cased well using a 3D cylindrical electromagnetic modelling code. Subsequently, we distribute a series of equivalent current sources along the well's trajectory within a complex 3D resistivity model. We then discretize this model using a tetrahedral mesh and simulate the borehole electromagnetic responses excited by the casing source using a 3D finite-element electromagnetic code. This multi-step approach enables us to simulate 3D casing source electromagnetic responses within a complex 3D resistivity model, without the need for explicit discretization of the well using an excessive number of fine cells. We discuss the applicability and limitations of this proposed workflow within an electromagnetic modelling scenario where an energized well is deviated, such as at the Frontier Observatory for

Research in Geothermal Energy site. Using the workflow, we demonstrate that the combined use of the energized casing source and the borehole electromagnetic receiver system offer measurable magnetic field amplitudes and sensitivity to the deep localized stimulated zone. The measurements can also distinguish between parallel-fracture anisotropic reservoirs and isotropic cases, providing valuable insights into the fracture system of the stimulated zone. Besides the magnetic field measurements, vertical electric field measurements in the open well sections are also highly sensitive to the stimulated zone and can be used as additional data for detecting and imaging the target. We can also acquire additional multiple-source data by grounding the surface electrode at various locations and repeating borehole electromagnetic measurements. This approach can increase the number of monitoring data by several factors, providing a more comprehensive dataset for analysing the deep-localized stimulated zone. The numerical analysis indicates that it is feasible to use the combination of the energized casing and downhole electromagnetic measurements in monitoring localized stimulated zone at large depths.

KEYWORDS
borehole geophysics, electromagnetics, modelling

INTRODUCTION

Enhanced geothermal systems (EGSs) are engineered reservoirs fractured to extract heat energy from low-permeability geothermal resources (Blackwell et al., 2006; Kneafsey et al., 2018). The concept behind EGS is relatively straightforward. The process involves drilling an injection well into hot rock having low permeability. Water is then injected into the reservoir, creating hydraulically fractured zones throughout the heat reservoir. This hydraulic stimulation enhances the permeability of the reservoir and enables the water to circulate through the fractured zones for heat exchange. A production well is then drilled into the fractured zones. Hot water and steam are extracted from the well for power generation. EGS is an important renewable energy technology being investigated for application in the Western United States and many other areas around the world (Breede et al., 2013; Dobson et al., 2020; Lu, 2018; Tester et al., 2006).

Monitoring the distribution of fractures and fluid saturation inside EGS over time is crucial for the efficient development and operations of geothermal systems (Kneafsey et al., 2018; Kolditz et al., 2012). By monitoring these and other parameters, engineers can identify areas of the reservoir that are underperforming and make adjustments to the injection and production rates, increasing the overall efficiency and long-term sustainability of geothermal energy production. Geophysical methods play a critical role in achieving these objectives. For instance, the microseismic method is capable of identifying the locations of microseismic events related to hydraulic fractures and outlining P- and S-wave velocity structures (Dyer et al., 2008; Lellouch et al., 2020; Oye et al., 2012). The V_P/V_S ratio obtained from these measurements can be utilized to map fluids and steam-saturated areas within the stimulated zone (Boitnott & Kirkpatrick, 1997; Gritto & Jarpe, 2014; Gritto et al., 2022; Lin & Wu, 2018; Moos & Zoback, 1983). However, microseismic-based mapping highly depends on initial velocity models, introducing uncertainties due to our limited understanding of these models. Microseismic events are often too small to be reliably recorded, resulting in uncertainties (Johnston & Shrallow, 2011). More importantly, the event locations do not necessarily indicate active fluid pathways (Hoversten et al., 2015), which is also a key consideration for efficient EGS operations.

In contrast, electromagnetic (EM) methods can be directly sensitive to electrical resistivity contrasts between low-resistivity water-saturated areas and high-resistivity impermeable host rocks, complementing microseismic methods in EGS sites and reducing uncertainty. For example, the magnetotelluric (MT) method has been a primary EM tool for locating potential geothermal structures at depth and has also been applied to monitor fluid flow at geothermal reservoir scale (Lindsey et al., 2016; Muñoz, 2014; Newman et al., 2008; Peacock et al., 2012, 2013, 2020, 2022; Wannamaker et al., 2004). In contrast, borehole-based EM methods have been used to detect fluid flow in the vicinity of wells at higher resolution and higher sensitivity (Börner et al., 2015; Castillo-Reyes et al., 2021; Cuevas, 2019; Wilt et al., 2002).

The US Department of Energy's (DOE) Utah Frontier Observatory for Research in Geothermal Energy (FORGE) is

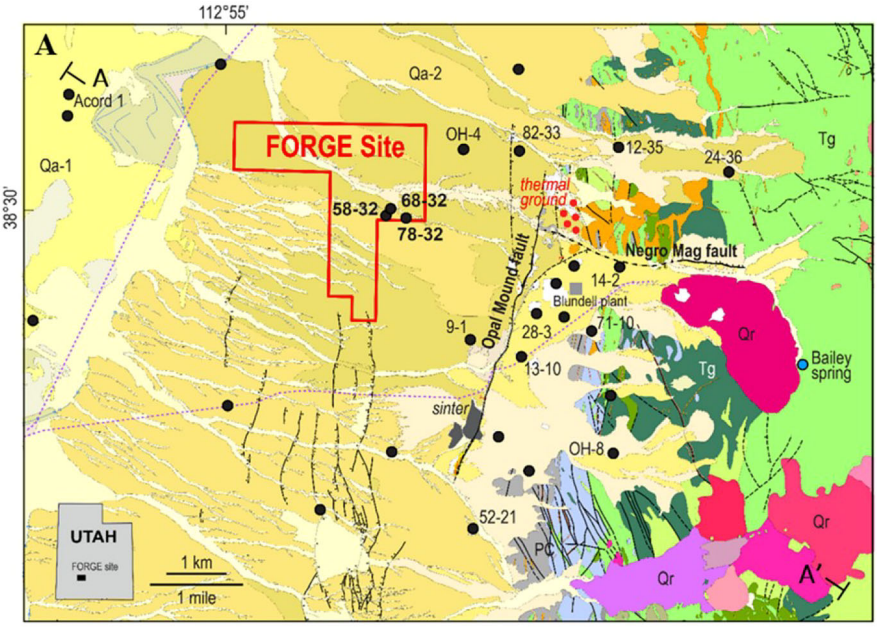

(a)

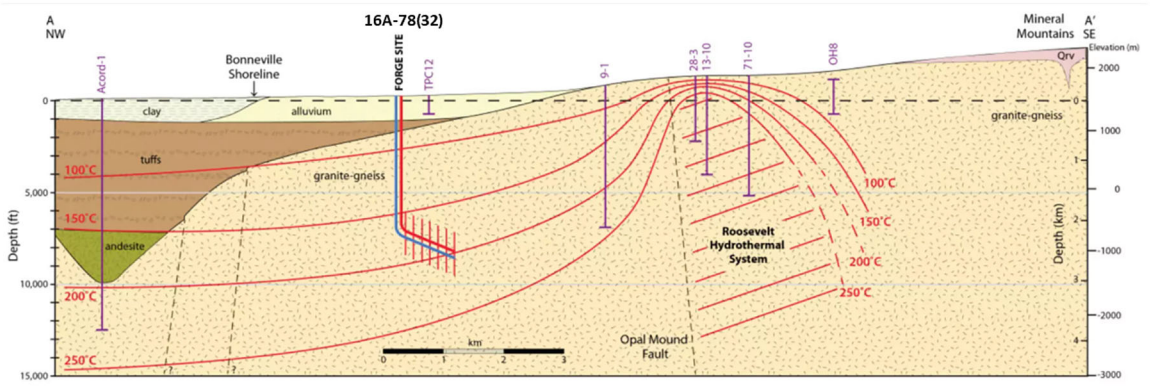

(b)

FIGURE 1 (a) Location map of the Frontier Observatory for Research in Geothermal Energy (FORGE) site in central Utah. (b) A cross-sectional view of the geology around the FORGE site (Wannamaker et al., 2020).

a field laboratory (Figure 1a) located in south-central Utah (Moore et al., 2019, 2020). The primary objective of the Utah FORGE laboratory is to provide a controlled environment for testing and developing new technologies that can monitor, characterize, create and sustain EGS. The area has been the focus of numerous geoscientific studies since the 1970s for geothermal development, specifically at the nearby Roosevelt Hot Springs. In 2017, a vertical scientific well (58-32) was drilled and tested to a depth of 2290 m at the FORGE site to provide additional characterization of the reservoir rocks.

As a participant in the Utah FORGE research programme, Lawrence Berkeley National Laboratory (LBNL) has been contracted to collect controlled-source EM data that will be used to characterize the stimulated geothermal reservoir. We note that the expected stimulated zone is highly localized (a few 100 m wide) at a depth of several kilometres. Given the depth to the reservoir coupled with the limited size of the simulated zone and expected increase in fracture porosity of only 1% (Finnila & Podgorney, 2020; Xing et al., 2022), it would be difficult or impossible for surface-based EM measurements to provide sufficient sensitivity to detect changes caused by the stimulation. Note that this has been verified by our initial numerical modelling studies that for space reasons have not been included here, as well as repeat MT measurements made before and after a test stimulation. To attempt to enhance the sensitivity, we will deploy a three-component borehole magnetic receiver system called vertical EM profiling (VEMP) system (Miura et al., 1996; Wilt et al., 1997) in observation wells. We provide a detailed description of the recently refurbished VEMP system later in this paper.

As shown in Figure 1b, the target zone for the numerical simulation is electrically resistive granitoid bedrock. The bedrock is in turn overlain by a 500–1400 m thick cover of low-resistivity layers. These geological conditions limit a conventional surface-based loop or dipole source to provide sufficient EM field that can penetrate down to the stimulated zone. To overcome this challenge, we plan to electrically energize the steel casings (Marsala et al., 2014) of the injection/production well, which provides for much larger source currents and stronger signals in the basement complex than can be achieved by a surface source. In this paper, we present a numerical feasibility study of a novel EM field measurement that combines the use of the VEMP system and energized casing sources for characterizing the deep-localized stimulated zone.

In general, it is numerically challenging to simulate/discretize a hollow steel-cased well in a 3D reservoir-scale or regional-scale EM earth model. For example, the 3D discretization of a steel-cased well in the rectangular coordinate system requires using a large number of fine elements/cells because a typical steel well casing is only millimetres to centimetres thick, whereas, at the same time, it is more than a million times more conductive than surrounding geology. The number of elements required for discretizing such a model with a well casing exponentially increases as the well length increases, making 3D EM modelling using the true casing dimensions intractable even on a large-scale parallel computer (Commer et al., 2015; Um et al., 2015). On the other hand, 3D cylindrical-mesh-based EM modelling codes (Heagy & Oldenburg, 2019) excel at accurately discretizing a hollow vertical cased well using a relatively small number of cells. However, the challenge arises when dealing with a complex 3D resistivity model, which cannot be reasonably discretized within the cylindrical coordinate system. Furthermore, when a well is deviated such as the injection/production wells at the Utah FORGE site, the high conductivity casing no longer aligns with the cylindrical coordinate system.

To address these challenges, we propose a 3D EM modelling workflow capable of simulating the energization of a vertical steel-cased well at a fraction of the computational cost required for explicit discretization. Instead of developing an entirely new modelling tool for casing source EM simulations, we adopt a synergistic approach by utilizing two existing 3D EM modelling codes: the 3D SimPEG code (Heagy & Oldenburg, 2019) and the 3D finite-element EM code (Um et al., 2020). By integrating the strengths of each code, we leverage their advantages for tackling casing EM modelling challenges. Once we demonstrate the accuracy and efficiency of the proposed workflow for a vertical well, we discuss its applicability and limitations when dealing with a deviated cased well, which we are interested in energizing at the FORGE site.

In this paper, we present and discuss simulations and the potential deployment of the VEMP tool at the Utah FORGE site when an injection/production well serves as an EM source. The objective of this paper is twofold. First, we introduce an EM modelling workflow designed for efficiently simulating the energization of steel-cased wells in a general 3D model and expand its application to a deviated well. Second, we provide a numerical modelling study of the proposed EM data acquisition scenario at the FORGE site. We hope that this study can serve as a useful guide for future research on the combined use of borehole EM receivers and energized casing source for geothermal characterization and other geophysical monitoring applications.

The rest of this paper is organized as follows. First, we introduce the newly refurbished VEMP system. To conduct a realistic feasibility study, we derive a 3D background resistivity model from an MT inversion at the FORGE site. Next, we determine the size and of the stimulated zone from 3D discrete fracture network modelling analysis as well as microearthquake hypocentre locations that we determined from a test stimulation conducted in April of 2022. The resistivity of the stimulated zone is then estimated using an equivalent medium theory approach suggested by Berryman and Hoversten (2013). Next, we present a 3D modelling workflow that converts a deviated energized well to a set of small electric dipole sources. Finally, using the modelling workflow and the 3D resistivity models, we simulate and evaluate the VEMP measurement configuration with an energized casing source for mapping the stimulated zone.

VERTICAL ELECTROMAGNETIC PROFILING SYSTEM

The vertical electromagnetic profiling (VEMP) system (Figure 2) was developed by ElectroMagnetic Instruments Inc (EMI) instruments in 1995 with funding from the Geothermal Energy Research and Development (GERD) of Japan. The system was designed for subsurface imaging, primarily for high-temperature borehole deployment in geothermal wells and mineral exploration (Alumbaugh et al., 2023; Miura et al., 1996; Wilt et al., 1997). The original system operated with separate stations that log independently but are linked by high-accuracy clocks. The transmitter typically injects a 1–30 Ampere current into either a surface electric bipole or loop antenna using frequencies ranging from 1 to 128 Hz. This current is logged synchronously with the borehole receiver signals using an inductive current monitor.

The VEMP receiver includes a borehole 3-component inductive sensor and a fluxgate magnetic orientation sensor. The axial sensor is 1.5 m long, with a 1 cm core made of magnetically permeable mu-metal. It is wrapped with tens of thousands of turns of wire and connected to a downhole

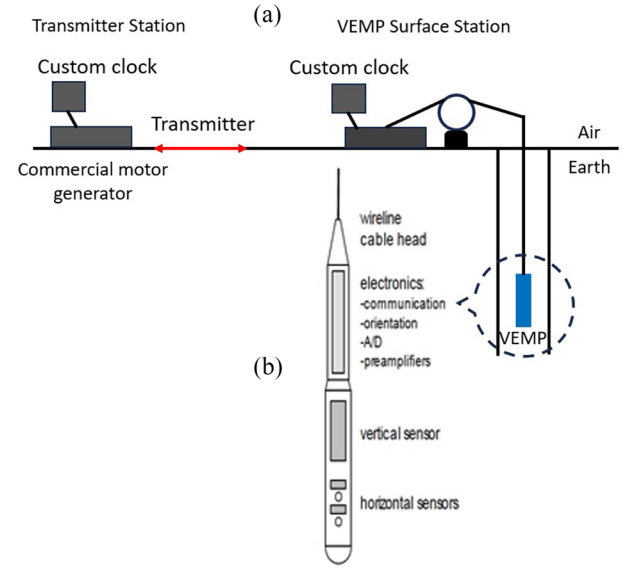

FIGURE 2 (a) The vertical electromagnetic profiling system (VEMP) surface to borehole field system. (b) The schematic of the VEMP borehole receiver. (c) Testing the deployment of the VEMP system at Richmond Field Station in Richmond, California, USA in 2023. The lower white section of the tool houses the sensors, whereas the upper metallic section contains the vacuum dewar containing the electronics.

amplifier in a magnetic feedback configuration. It has excellent sensitivity ranging from 1 to 300 Hz. The horizontal magnetic components are measured using an array of transverse orthogonal sensor coils connected in series with parallel feedback windings. These coils provide high sensitivity and temperature stability in a small package. The noise floors for the vertical and horizontal magnetic field sensors are 10^{-14} and 10^{-13} T, respectively. As shown in Figure 2, the original design of the VEMP system was for surface-to-borehole configuration. However, due to the depth and size of the anticipated stimulated zone and electrical conductivity structures at the Frontier Observatory for Research in Geothermal Energy (FORGE) site mentioned earlier, we plan to use the VEMP system along with an energized casing source.

The VEMP system can tolerate temperatures up to 260°C. Its internal preamplifiers, power supply and digital electronics are placed inside a custom vacuum dewar designed to provide the tool with 18 h of operation in a high-temperature borehole environment. With its high-sensitivity three-component magnetic sensor, the VEMP system is well-suited for detecting fractures. The VEMP system has maximum sensitivity at low frequencies between 1 and 300 Hz, allowing for large source-receiver separations. It can operate in open hole or within steel well casing though operation in steel casing requires the data to be corrected for the casing effects (Gao et al., 2008; Wu & Habashy, 1994).

BUILDING 3D ELECTRICAL RESISTIVITY MODELS WITH AND WITHOUT STIMULATED RESERVOIR ZONES

The baseline resistivity model is derived from the 3D magnetotelluric (MT) inversion results of Wannamaker et al. (2020). This involved the inversion of 122 processed MT sites that were collected over Utah FORGE site and the surrounding area. The inversion was accomplished via a finite-element (FE) code (Kordy et al., 2016) that employs deformed hexahedral meshes in order to properly account for the rugged basin and range topography (Figure 1). In contrast, the controlled-source EM numerical modelling algorithms (Um et al., 2020) chosen for this study involve the use of structured rectangular or unstructured tetrahedral elements. To adapt the existing model to needs in this study, we have mapped and interpolated 3D results of Wannamaker et al. (2020) from deformed hexahedral meshes to regular rectangular meshes. This resulted in the models shown in Figure 3 where the rectangular mesh consists of 80 cells in both the horizontal directions, and 240 cells in the downwards direction. In the central part of the mesh where the borehole EM fields are to be evaluated, model cell sizes in the horizontal directions are 50 m and start at 10 m in the downward direction at the surface to better account for topography and slowly increase to 50 m at depth. Figure 4 illustrates the coordinate system of the FORGE resistivity model and provides additional information on elements such as injection and observation wells employed in this modelling study.

In order to calculate the resistivity of a hypothetical stimulated zone generated by fracturing the granitic basement rock, we used the effective medium theory algorithm devel-

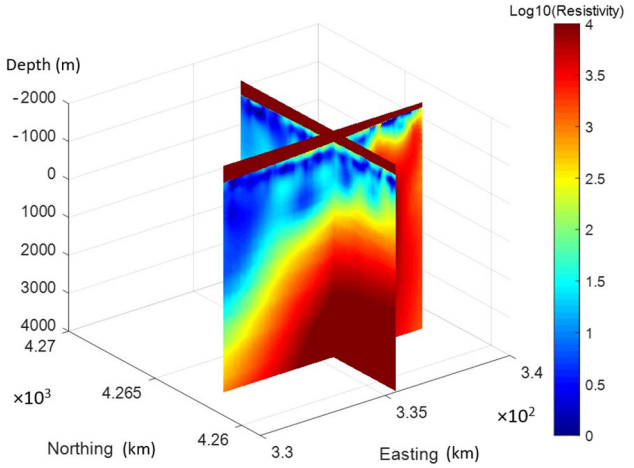

FIGURE 3 The 3D electrical resistivity model derived from the 3D magnetotelluric (MT) inversion at the Frontier Observatory for Research in Geothermal Energy (FORGE) site (Wannamaker et al., 2020).

oped by Berryman and Hoversten (2013). This computational approach requires a set of input parameters, including geometric characteristics of the fractures (e.g. radius and thickness), their volume fraction in each of the x, y and z directions and the electrical conductivity of the pore fluid within the fractures. The algorithm assumes that the fractures consist of a series of penny-shaped cracks filled with electrically conductive fluid that are embedded in an otherwise homogenous medium. For the Utah FORGE site, we assumed this background medium to be that of the granitoid with a resistivity of 3000 Ω m. The radius of the cracks and their thickness was set to 10 m and 2 mm, respectively, aligning with the distribution used for the discrete fracture network (DFN) modelling at the FORGE site (Finnila & Podgorney, 2020). The water that will be employed during the stimulation to generate the enhanced geothermal system (EGS) is treated water, and it is assumed to possess a salinity level of 400 ppm. A measured temperature at the depth of the stimulated zone was 218°C. Combining these parameters yields a water resistivity of 2 Ω m (Schlumberger, 2005). Once these parameters are provided, the algorithm iteratively computes anisotropic electrical conductivities using a depolarization tensor formulation. For a comprehensive description of the algorithm, readers are directed to the reference mentioned above.

As mentioned above, the effective medium algorithm allows a user to orient cracks in the space. Note that for describing the fracture orientation here, we employ a local coordinate system highlighted in red, as depicted in Figure 5. In the first case (fracture model 1), we assume that all fractures are filled with the electrically conductive fluid and are oriented only perpendicular to the x-axis (i.e. the y–z plane). This yields an electrically anisotropic reservoir with a resistivity in the x direction of 2970 Ω m, and in the y and z directions, the computed resistivity is 190 Ω m. The second case (fracture model 2) is based on the statistics (Table 1) for four different sets of fractures that were derived from the DFN modelling (Finnila & Podgorney, 2020), in which 28% of the fracture have an orientation in the x–y plane, 32% in the x–z plane and 40% in the y–z plane. Using these statistics yielded a more isotropic resistivity with values of 302 Ω m in the x direction, 270 Ω m in the y direction and 256 Ω m in the z direction. We create two different reservoir models using these different sets of fracture-zone resistivities in order to determine if there will be sufficient sensitivity within the EM measurements to whether the stimulated reservoir is isotropic or anisotropic. To better understand the changes that occur during stimulation, we present two cross-sectional views of the electrical resistivity models before and after stimulation along profiles A–A′ and B–B′ which are marked on a location map in Figure 4. As mentioned earlier, the baseline model (Figure 5a) is derived from the MT inversion model (Wannamaker et al., 2020). Then, the model is used to fill a volume with the reservoir dimensions given above to represent a model after stimulation (Figure 5b).

ELECTROMAGNETIC MODELLING OF ENERGIZED STEEL-CASED WELL

As previously mentioned, a major numerical challenge in this feasibility study is to simulate the EM effects of an energized steel-cased well in the 3D FORGE model, where the lower part of the injection well which we want to energize is deviated as shown in Figures 1b and 5. Note that this geometry does not fit within a cylindrical coordinate system that we will be using to simulate current conduction in a steel well casing. Directly discretizing this source well geometry in the 3D rectangular coordinate system requires an extremely large number of fine elements, which often exceeds the capabilities of mesh generation software and/or available computational resources.

To tackle this numerical challenge, we propose a modelling workflow that first approximates the EM effects of an energized steel-cased well when the well is vertical. Then, we discuss the applicability and limitations of the workflow to a deviated well. The workflow consists of four steps. First, we construct a layered Earth model whose resistivity structure is consistent with resistivity that exists along the trajectory of a vertical well (Step 1). Accordingly, we need to have a 3D resistivity model of the area of interest which, in this case, is the resistivity model shown in Figure 5a. Resistivity logging data can also be utilized here to create a more detailed layered model along the well bore. However, in many cases, logging data do not extend all the way from the surface to the bottom of the well but are collected only for a small section of the well. Accordingly, a large portion of the layer Earth

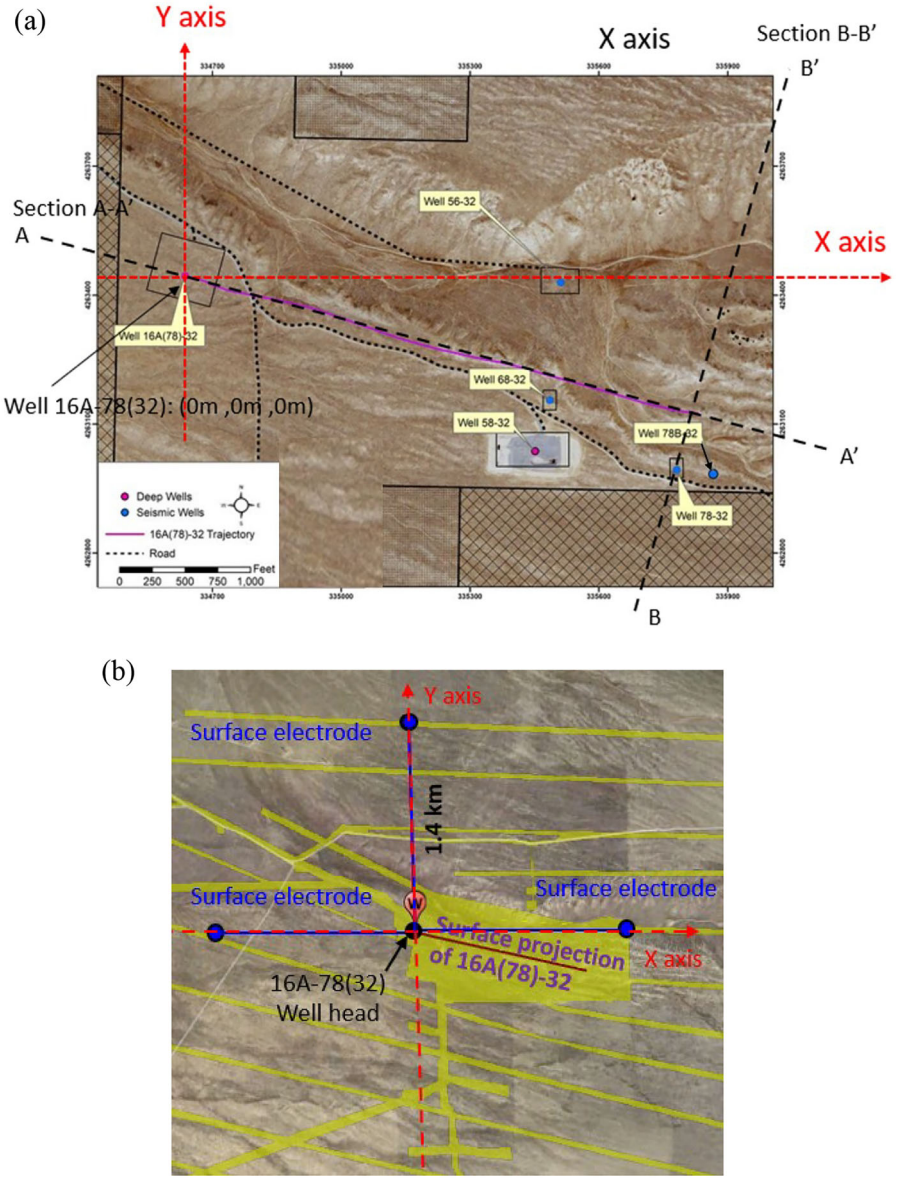

FIGURE 4 (a) The Utah Frontier Observatory for Research in Geothermal Energy (FORGE) map (https://utahforge.com/) showing the injection well 16A(78)-32 and other observation wells. The red broken lines indicate a coordinate system with the centre set at the wellhead of the injection well. The trajectory of the deviated part of the injection well is indicated by the magenta line. (b) Map view of the site shows that the three different surface return electrode positions are used in this paper. A downhole electrode is connected to the inside of well 16A(78)-32 at either 500 or 1000 m in depth as illustrated in Figure 5. Yellow lines denote accessible roads.

TABLE 1 Statistics for four-sets of fractures used for the discrete fracture network (DFN) modelling at the Frontier Observatory for Research in Geothermal Energy (FORGE) site (personal communication with Finnila).

	Orientation		Intensity	
Set description	**Mean trend/plunge (degree)**	**Mean strike/dip (degree)**	**P_{32} (1/m)**	**(%)**
South striking moderately dipping west	88.5/46	178.5/44	0.42	36.1
East striking steeply dipping south	1.5/13.5	91.5/76.5	0.35	30.1
North striking steeply dipping east	260/17	350/73	0.20	17.2
SSW striking vertical	131/5	221/85	0.19	16.6
			1.15	100.0

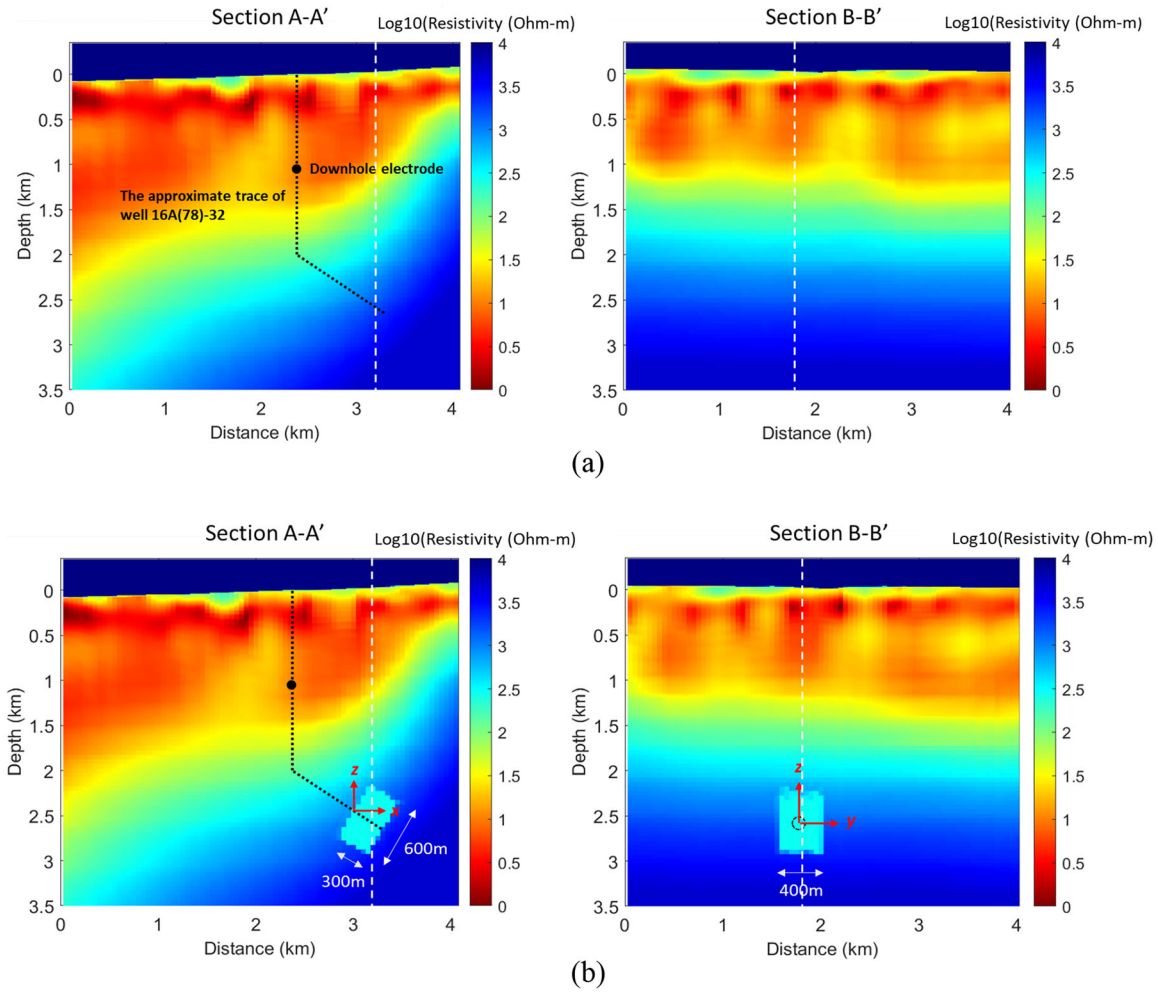

FIGURE 5 Cross-sectional views of the 3D electrical resistivity (a) before and (b) after stimulation along Sections A–A′ and B–B′ shown in Figure 4a. The red axes shown in (b) represent a local coordinate system utilized to describe the fracture geometry and orientation. The white vertical broken lines denote the intersection of the Sections A–A′ and B–B′. Note that the fracture zones are anisotropic. However, for the sake of straightforward visualization, the resistivity of the fracture zone above is set to 256 Ω m, the resistivity of fracture model 2 in the z direction.

model still needs to be estimated from either geology or EM inversion models.

Next, we simulate electrically energizing the vertical well using a 3D EM modelling code supporting the cylindrical coordinate system (Step 2). This simulation can be done at low computational costs (e.g. less than an hour on a high-end workstation computer available in 2023) because the vertical well naturally fits within the cylindrical coordinate system and does not require an excessively large number of fine cells/elements. After these simulations, we extract the vertical electric current density along the outer surface of the well (Step 3). Previous researchers (Cuevas, 2014; Kohnke et al., 2018; Tang et al., 2015) have shown that the variation of the current density along the well can approximated by a series of equivalent dipole sources. This set of equivalent dipoles is then mapped along the trajectory of the well in the 3D earth model (Step 4), which, in this case, is discretized using tetrahedral meshes. Unlike cylindrical meshes, the tetrahedral meshes are better suited for discretizing complex resistivity structures.

Here, we make the simplifying assumption that the well has a uniform single casing thickness from top to bottom. Additionally, we assume a uniform current density across the cross-sectional area of the casing at each depth within the well, allowing us to compute the total casing current at any given depth by multiplying the cross-sectional area of the well with the current density on the outer surface of the well. It is important to note that this assumption of uniform casing current distribution does not hold when the casings are nested, leading to variations in current distribution across the cross section (Beskardes et al., 2021). In this scenario, it becomes necessary to model the well-completion design and compute the casing current at a specific depth by performing an integration of the current density over the entire cross-sectional area.

To implement this workflow, we have not developed new numerical modelling codes. Instead, we use widely used and

proven EM modelling codes that are available to us. Later, we describe how the numerical modelling codes are used for the workflow. We simulate an energized verticalized steel-cased well using 3D SimPEG codes (Heagy & Oldenburg, 2019). SimPEG is an open-source Python package for simulation and gradient-based parameter estimation in geophysical applications. Although most 3D EM geophysical modelling algorithms use the 3D Cartesian coordinate system, SimPEG also supports a cylindrical coordinate system and can discretize a vertical well accurately without excessive mesh refinement. In this paper, we assume a uniform single casing structure for ease of modelling, but the 3D SimPEG code can also discretize a nested casing model if a well-completion design is available.

To verify the accuracy of the casing current density calculated by the SimPEG code, we first compare casing current solutions between the SimPEG and a method of moments (MoM) solution (Tang et al., 2015). The goal of this step is to ensure the quality of the computational mesh for SimPEG's casing model through this comparative analysis. To create the mesh, we employ SimPEG's default casing mesh generator. For details, readers are referred to Heagy and Oldenburg (2019). Note that the current version of the MOM code supports only the top-casing source configuration, where one electrode is connected to a wellhead and the other is grounded at a certain distance from the well. In addition, the MoM code is limited to a vertical well and homogeneous half-space model. Therefore, we compare the casing current density vectors along a vertical well, computed by both MoM and SimPEG with the top-casing source configuration, across various background resistivity values extracted from the layered model employed by the SimPEG model.

For example, Figure 6a shows the casing current density calculated using the MoM and SimPEG codes. In this specific scenario, a steel-cased well is 1 km deep, and the source electrode is connected to the top of the well casing (electrical conductivity: 10^6 S/m; outer radius: 0.1 m, thickness: 0.02 m). The return electrode is located 2 km away from the wellhead. The source is operating at 1 Hz, and the earth resistivity model is a 100 Ω m homogeneous half-space. The well is discretized into 200 cells in both MoM and SimPEG model. As demonstrated in Figure 6, the casing current plots from both methods show good agreement with each other. We also note that it is worth mentioning that the modelling labour and computational costs associated with MoM and SimPEG solutions are not substantial. Both modelling tools enable users to quickly construct a casing EM model, and the MoM and SimPEG solution processes can be completed in just a few minutes and a few tens of minutes, respectively, when using a high-end workstation computer.

Until now, we have shown that sufficiently accurate casing currents can be derived from the SimPEG casing model. Now, we examine whether these extracted casing currents can effectively replace the steel-cased well in a 3D earth model. The goal of this examination is to construct high-quality 3D mesh based on rectangular coordinates, capable of accommodating the set of casing current densities and producing casing EM responses at borehole receivers. To do this, we compare the 3D borehole EM responses between the true casing source (i.e. SimPEG solutions) and the equivalent current density sources. We utilize a 3D FE EM modelling code (Um et al., 2020), which discretizes the model using unstructured tetrahedral meshes, aligns tetrahedral edges along the trajectory of the energized casing well, distributes the equivalent sources along the trajectory and computes EM solutions. For details on the algorithm and mesh design, readers are referred to Um et al. (2020). Figure 6b displays the comparison of the EM fields from the two solutions for an observation well located 500 m away from the energized casing, showing a good agreement between the two.

The idea of replacing an energized cased well with a set of small equivalent current sources is not entirely new. The approach has been previously examined, and its limitations have also been discussed (Cuevas, 2014; Kohnke et al., 2018; Orujov et al., 2022; Tang et al., 2015). For instance, although the distribution of casing currents is strongly governed by the immediate surroundings, it can also be impacted by the surrounding 3D geology, introducing some level of uncertainty in the equivalent current source approach. We consider this limitation important, when 3D targets like fracture zones or injected fluid plumes are in proximity to the source well. Nevertheless, the suggested workflow offers a practical solution to this casing modelling challenge. The workflow combines the advantages of recent advancements in casing EM modelling algorithms and offers a more versatile approach to cased well EM modelling. For example, by utilizing the 3D cylindrical EM code, we can simulate more detailed casing properties and geometry (e.g. different EM properties for each casing segment, nested casing structures and others) and extract the resulting casing currents. By mapping the casing current densities into a 3D tetrahedral-based EM model, we can simulate EM casing source responses to a 3D resistivity earth model discretized in the rectangular coordinate system.

To this point, we have demonstrated that casing current densities can be extracted from the SimPEG's cylindrical mesh-based model and can be employed to accurately compute casing source responses within a 3D FE mesh-based model in the rectangular coordinate system. It is worth noting that the workflow has been applied to a vertical well rather than a deviated well, such as an injection well at the FORGE site (as shown in Figure 5). Accordingly, it is natural to ask whether this workflow can be applied to a deviated well. In this modelling scenario, we construct a layered model whose resistivity structure is consistent with resistivity along the trajectory of the deviated injection well 16A(78)-32 in the 3D FORGE MT model. Figure 7 shows the electrical resistivity

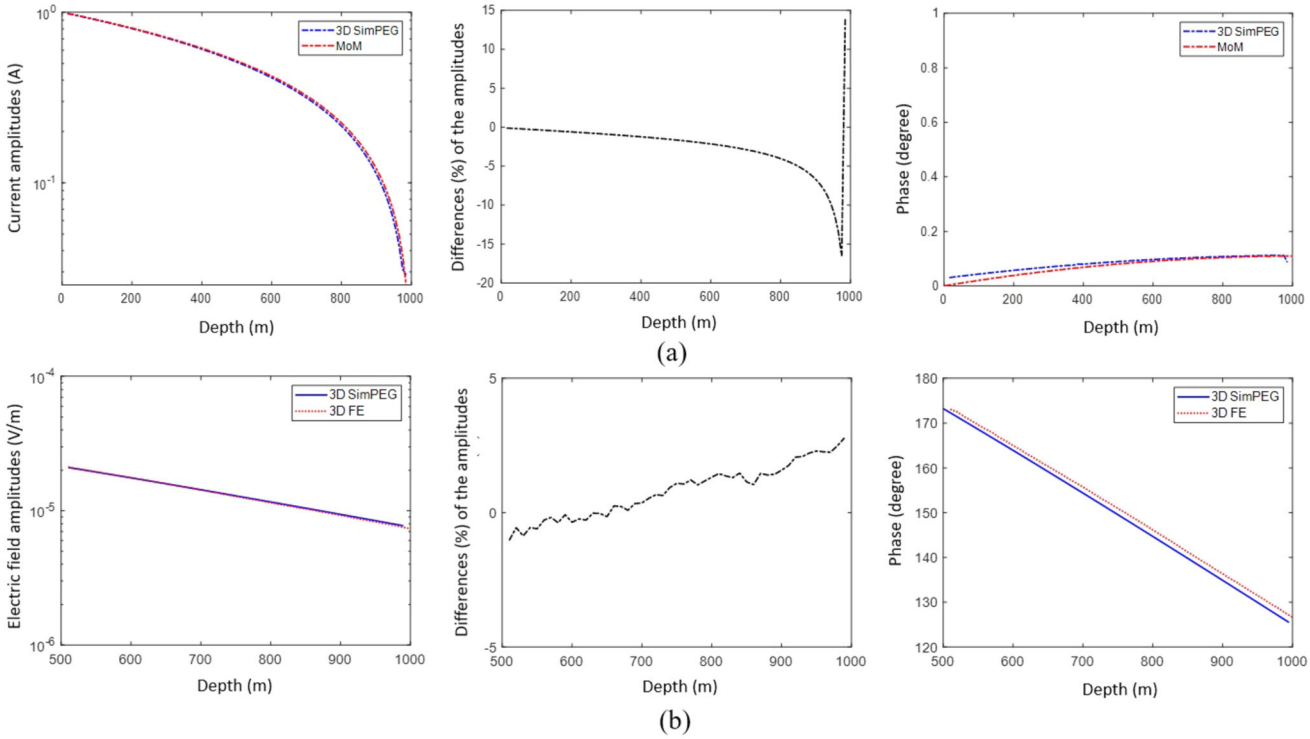

FIGURE 6 (a) Comparisons between the current density vectors (complex quantities) calculated along the source well using the 3D SimPEG and method of moment (MoM) method. The *x*-axis represents the source well depth. (b) Comparisons between borehole electromagnetic (EM) responses in an observation well, calculated using true casing geometry (SimPEG) and equivalent sources (3D finite-element [FE] solutions). The *x*-axis represents a receiver position in the observation well. The middle column displays the relative differences between the plots shown in the left column. The steel-cased source well is 1 km deep, and the source electrode is connected to the top of the well casing (conductivity: 10^6 S/m; outer radius: 0.1 m, thickness: 0.02 m), and the return electrode is located 2 km away from the wellhead. The source is operating at 1 Hz, and the Earth model is a 100 Ω m homogeneous half-space.

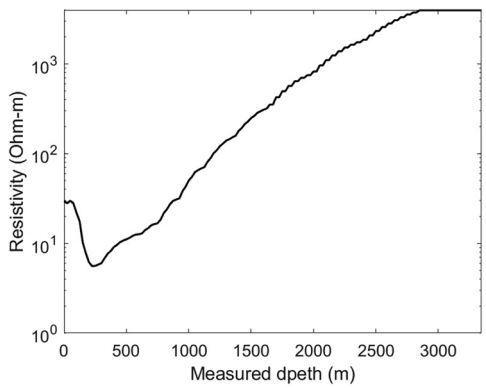

FIGURE 7 The electrical resistivity structures along the injection well extracted from the magnetotelluric (MT) model (Figure 3). Note that the *x*-axis does not represent true vertical depth but rather the measured depth along the trajectory of the well.

structures along this injection well, as extracted from the MT model. Next, we insert a vertical steel-cased well, whose depth is the same as the measured length (3349 m) of the deviated well, into the layered model. Third, we simulate energizing the verticalized well using the 3D SimPEG code. Finally, the casing current densities are extracted from the SimPEG model and distributed along the true trajectory of the deviated well in the 3D earth model. Figure 8 figuratively summarizes the process of mapping the current density vectors from a vertical well to the actual deviated well trajectory.

A key question here is whether or not the casing current distribution derived from a verticalized steel-cased well can represent the casing current distribution for a corresponding deviated well. In general, the current distribution derived from a verticalized well might not always closely resemble that of its true deviated well counterpart because of the differing impact that a return electrode grounded on the surface has on casing currents in vertical versus deviated wells.

To the best of the authors' knowledge, there is currently no analytical algorithm available to calculate the casing current distribution along a deviated L-shape well (Figure 5) energized by a downhole electrode. Directly applying the 3D FE algorithm for discretizing and simulating the entire 3 km length of the deviated L-shape well is also computationally intractable. Therefore, there are no modelling methods available to directly compare the casing current distribution

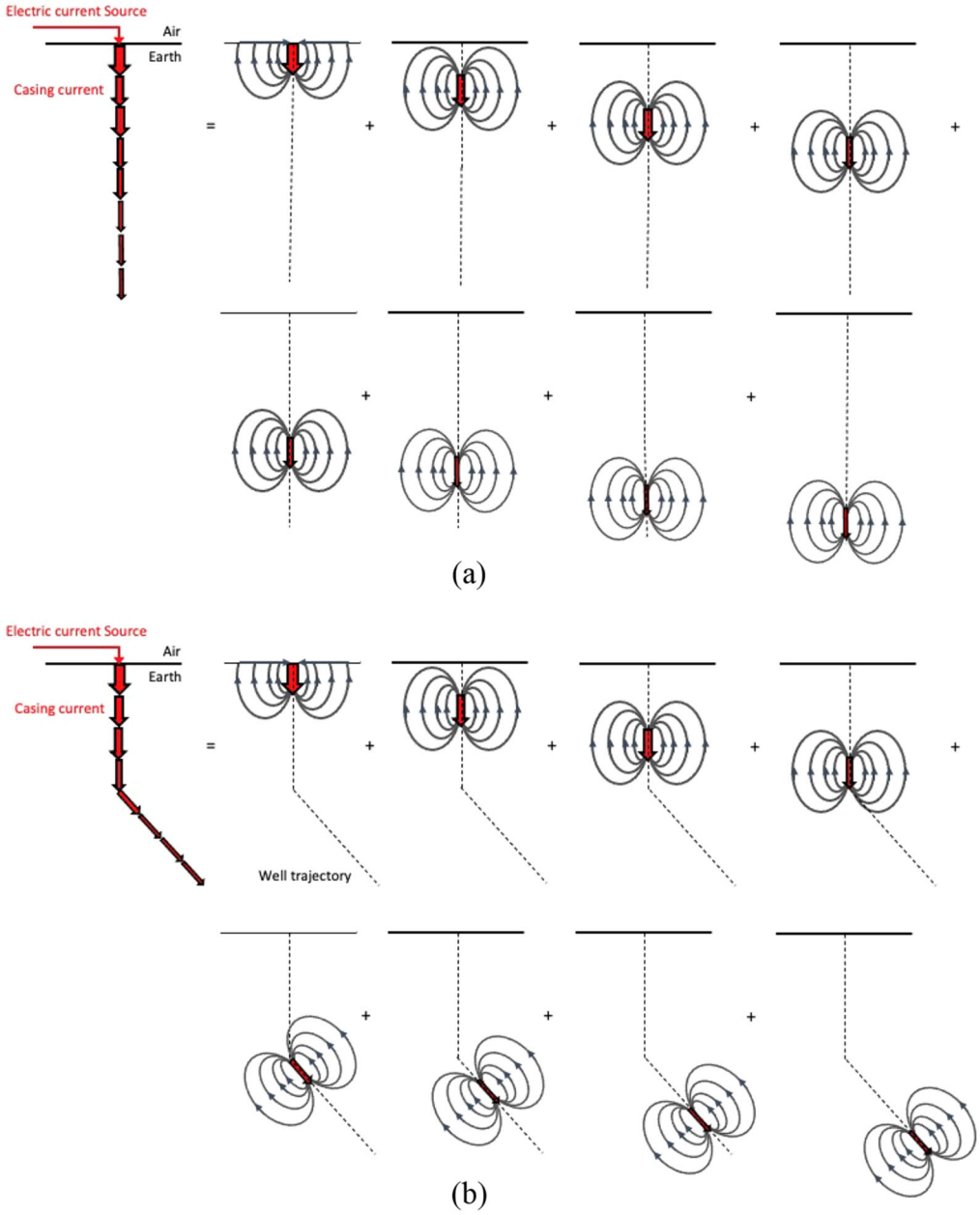

FIGURE 8 Mapping casing current density vectors from (a) a vertical well to (b) a deviated well. The red arrows indicate current density vectors, and the arrow thickness represents magnitude. For visualization purposes, (a) shows only eight dipoles, but in reality, the casing current is discretized using a number of small electric dipoles of varying amplitude and phase.

between the true deviated well and its verticalized counterpart. Alternatively, to provide a proof-of-concept verification of the proposed approach, we employ a hierarchical modelling method (Weiss, 2017) that can approximate the casing current distribution along the deviated well. The modelling approach represents the hollow steel-cased well by assigning casing conductivity values to the volumeless edges of the trajectory of the well, avoiding the need for excessive volume discretization using fine cells. Subsequently, we compare the hierarchical modelling solutions with the casing currents along a verticalized well calculated using 3D SimPEG in the cylindrical coordinate system. The comparison in Appendix 1 shows good agreement between the two solutions, indicating that the verticalization of a deviated well can serve as a practical first-order approximation tool.

In the context of the FORGE site, several factors lead us to further conclude that the above workflow will be effective for this site: (1) A highly conductive steel-cased well is embedded into a highly resistive granitoid bedrock, (2) the shallow area where the well is vertical is covered with conductive sediments, (3) the downhole electrode is positioned at a substantial depth (i.e. 1 km) beneath the surface, and (4)

a return electrode on the surface is grounded sufficiently distant (i.e. 1.4 km) from the well. Accordingly, it is reasonable to assume that the primary factor governing the casing current distribution and how slowly the current 'leaks' off of the casing into the formation is the resistivity contrast between the casing and the background geological formation rather than the position of the return electrode or other acquisition factors. In this context, it is logical to infer that the current distribution along a vertical well can represent the current distribution for the actual deviated well as long as the correct formation resistivity is used along the well. Although we acknowledge that our proposed workflow may not encompass all the details associated with the FORGE site, we think that it can serve as a valuable first-order approximation for assessing the sensitivity of the combined use of the energized casing source and the VEMP system to detecting changes at depth that are generated by EGS stimulation processes that are planned for the FORGE site. Thus, in the following sections, we focus on the FORGE EGS reservoir modelling scenarios.

SENSITIVITY OF BOREHOLE ELECTROMAGNETIC MEASUREMENTS TO STIMULATED ZONE

We evaluated three different casing source configurations for this study. The first configuration known as the top-casing source configuration (Marsala et al., 2014) employs a surface electric source. In this setup, one electrode energizes a wellhead, and the other is placed at some distance from the well. The second configuration is the downhole source configuration (Marsala et al., 2014) in which one electrode is directly connected to the casing within the well at depth, whereas the other electrode is placed on the surface. The third source configuration (Cuevas, 2014, 2019) uses a finite-long vertical electric dipole source inside the cased well. Through numerical modelling studies, we found that the top-casing source configuration is relatively less effective at the FORGE site because of the thick conductive overburden through which much of the currents injected at the wellhead leaks off from the well before reaching the target depth. In comparison, the downhole source configuration can deliver more currents to the target depth and illuminate a deeper target at the expense of a well-intervention procedure. The third configuration also provided some sensitivity but its EM field amplitudes were much smaller compared to those in the other two configurations. Therefore, this paper focuses on the downhole source configuration.

We examine the sensitivity of the VEMP system to the fracture models as a function of the downhole source depth. First, we compare three-component magnetic field and vertical electric field measurements with and without the stimulated zone when a downhole electrode is connected to the inside of the cased injection well at two different depths: 500 and 1000 m. For simplicity, we assume that the diameter and thickness of the casing are uniform from the top to the bottom rather than considering a complexly nested cased well. The outer diameter and thickness of the casing are set to 0.2 and 0.02 m, respectively. We also assume that the electrical conductivity of the steel-cased well remains constant and is set to 5×10^6 S/m. The return electrode is grounded 1.4 km away from the wellhead of the injection well at (0, 1.4 and 0 km) as shown in Figure 4b.

We assume that the casing's relative magnetic permeability is equal to one. However, it is important to note that carbon steel casing, which is commonly used in the oil, gas and geothermal fields, typically has a relative magnetic permeability that ranges from 50 to 200 (Gao et al., 2008). At 50 Hz, the effects of the magnetic permeability of energized steel casing on borehole EM measurements cannot be ignored, and it must be taken into account during modelling and data interpretation. Incorporating the effects into 3D EM modelling and inversion in a computationally practical manner is an ongoing research topic that goes beyond the scope of this paper. Although this paper focuses on the sensitivity of borehole EM responses to fractures excited by an energized casing source, we briefly demonstrate the effects of casing's magnetic permeability on borehole EM data and discuss potential methods for accounting for the effects in Appendix 2.

To assess the sensitivity of the combined use of the energized casing source and the VEMP system, we set two conditions: First, the proposed EM acquisition configuration should provide at least a 10% amplitude anomaly between modelling data calculated with and without the stimulated zone. Second, the field amplitudes should be sufficiently larger than the known sensor noise levels of the VEMP system (i.e. 10^{-14} T for vertical magnetic fields and 10^{-13} T for the horizontal magnetic fields). We simulated the EM responses at multiple frequencies ranging from 1 to 100 Hz and here present those at 50 Hz where observed fields sufficiently meet both the amplitude and anomaly conditions. We used amplitude anomalies to gauge sensitivity in this numerical study. The primary objectives are to demonstrate that the signal surpasses the noise and that an amplitude change is also significant enough to exceed the noise level. However, in practical data and inversion processes, we will utilize both amplitude and phase data (or real and imaginary data).

The VEMP system is deployed in observation wells 58-32 and 78B-32 (Figure 4). The VEMP system can measure magnetic fields in open or steel-cased well sections, though measurements made in the steel casing will be attenuated (Wu & Habashy, 1994). We place the VEMP system in the cased section of the wells (i.e. from 1500 to 2300 m in depth for well 58-32 and from 1700 to 2600 m for well 78B-32). At these depths, the diameter of well 78B-32 is large enough to accommodate the VEMP system; we have recently determined that

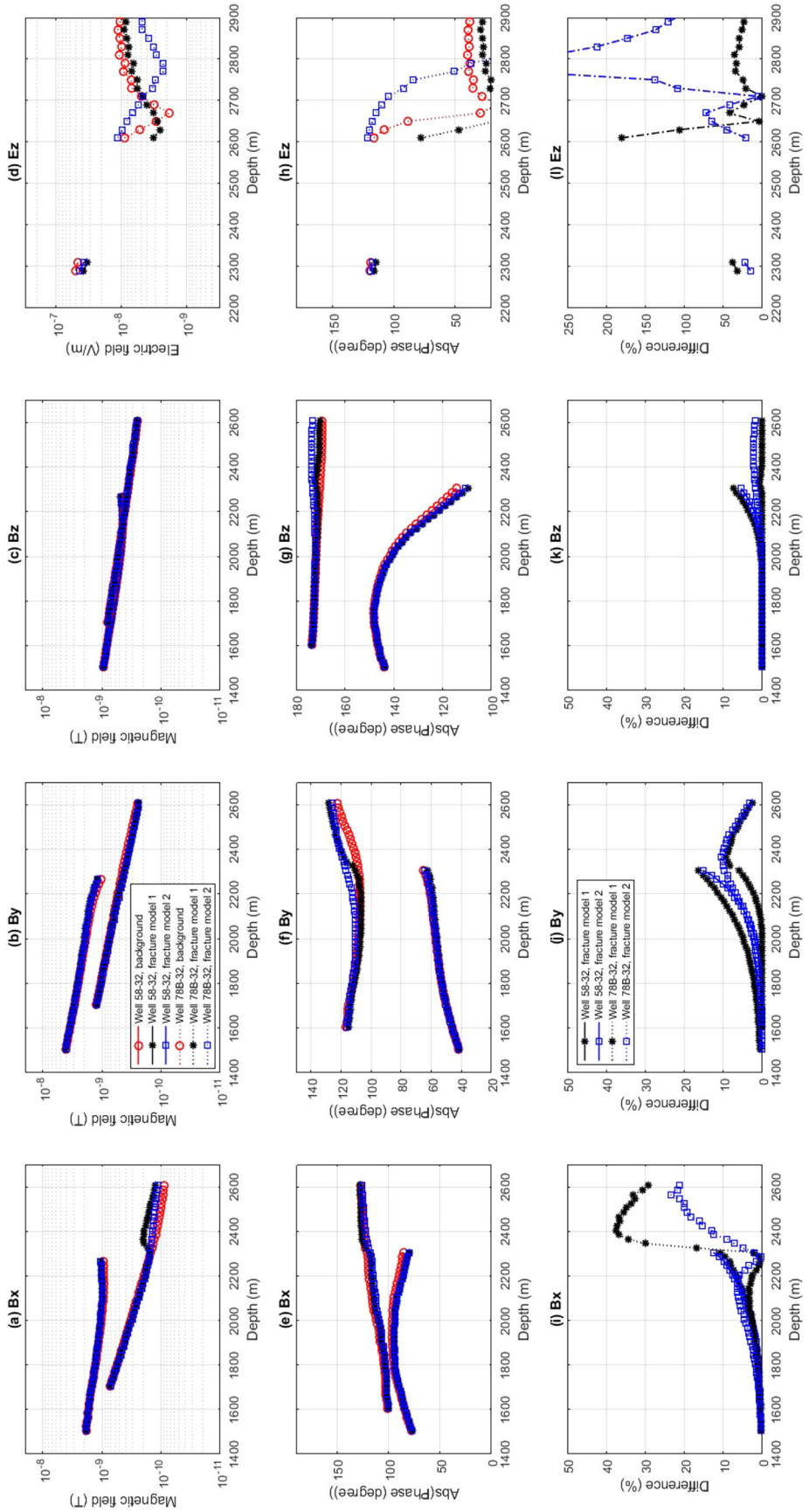

FIGURE 9 Comparison in simulated electromagnetic (EM) amplitude measurements (first row [a–d]) at 50 Hz before and after stimulation, the phase (second row [e–h]) and their relative amplitude differences (third row [i–l]). Three components of the magnetic fields (first to third column) and the vertical electric fields (fourth column) are plotted. The surface electrode is grounded at (0, 1.4 and 0 km), and the downhole electrode is connected to the inside of the casing at (0 km, 0 km and 500 m).

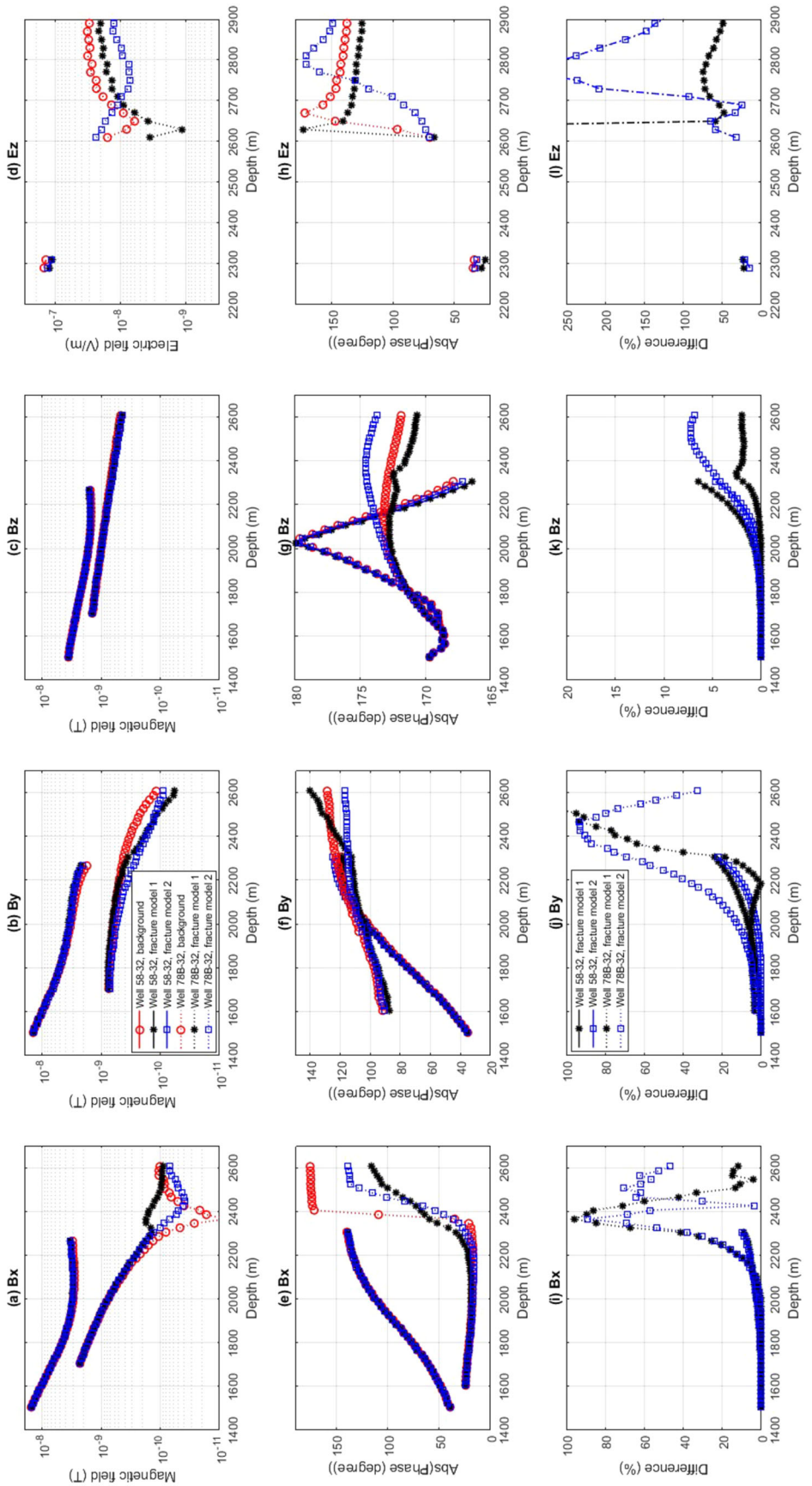

FIGURE 10 Comparison in simulated electromagnetic (EM) amplitude measurements (first row [a–d]) at 50 Hz before and after stimulation, the phase (second row [e–h]) and their relative amplitude differences (third row [i–l]). Three components of the magnetic fields (first to third column) and the vertical electric fields (fourth column) are plotted. The surface electrode is grounded at (0, 1.4 and 0 km), and the downhole electrode is connected to the inside of the casing at (0, 0 and 1 km).

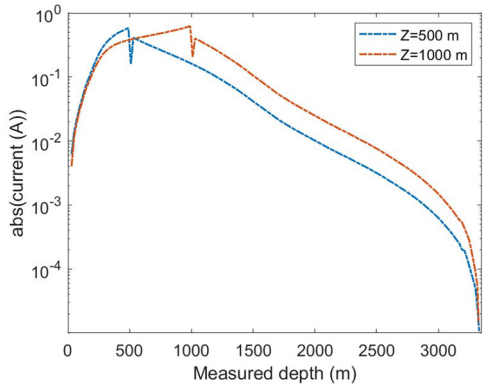

FIGURE 11 Comparison of casing current distribution along the well when employing two different depths of downhole electrodes. The *x*-axis represents the measured depth along the trajectory of the well. Casing current values are computed as averages over 5-m intervals along the length of the cased well. The casing source is represented using 670 dipoles within the 3D model.

the casing of well 58-32 is the same diameter as that of the VEMP tool (5″) suggesting that we will not be able to deploy VEMP in this well.

In order to provide a comprehensive analysis, we also simulate vertical electric field measurements. In practice, the electric fields can be measured using a vertical electric dipole, which is electronically simpler compared to a sophisticated coil-based borehole magnetic field sensor. However, it is important to note that electric fields can only be measured in the open well section, whereas the magnetic fields can be measured in both open and cased well sections. Due to the limitation, the electric fields are computed at two depths below the casing shoe of well 58-32 which has 33 m of open hole at the bottom of the well, and a range of positions over 300 m at the bottom of well 78B-32.

Figure 9 shows the borehole EM measurements at the two observation wells when the downhole electrode is connected to the inside of the injection well at $z = 500$ m. To take into account the attenuating effects of steel casing on VEMP measurements, we multiplied the magnetic field solutions by a complex casing attenuation coefficient as presented in Wu and Habashy (1994). Although the electric fields are measured in the open well, it is important to note that the presence of the steel-cased well above the electric dipole receiver may introduce distortions in the electric field measurements. On the other hand, we expect that the injection and observation wells, other steel-cased wells and steel infrastructure may minimally interact with each other because they are substantially isolated from each other. However, the extent and magnitude of these influences have not been addressed in this study and remain a subject for future research.

Regarding the EM field amplitudes shown in Figure 9, notice that they are several orders of magnitude larger than the noise levels discussed earlier. This is despite setting the source current amplitude to 1 A, and attenuating the magnetic fields measured in casing by the aforementioned casing coefficients. We expect field amplitudes to be significantly higher in practice as we anticipate transmitting between 5 and 20 A into the casing source. Thus, we conclude that borehole EM fields will be large enough to be measured.

The horizontal magnetic fields (i.e. the first and second columns of Figure 9) indicate that they can not only detect the stimulated zones but can also distinguish between the electrically anisotropic reservoir (fracture model 1) and the isotropic case (fracture model 2). The vertical electric field measurements are also highly sensitive to both the presence and anisotropic nature of the stimulated zone. This suggests that, along with VEMP measurements, vertical electric field measurements can serve as additional constraints for detecting and imaging the reservoir. As the downhole electrode position is moved from $z = 500$ to 1000 m, the amplitudes and sensitivity of the borehole EM measurements (Figure 10) increase further. For example, the horizontal magnetic field measurements (Figure 10i,j) provide up to 100% amplitude anomaly between the background and fracture models.

Figure 11 compares casing current distribution along the well, specifically examining the effects of deploying a downhole electrode at two depths: $z = 500$ m and $z = 1000$ m. The results clearly demonstrate that positioning the electrode at the deeper location significantly enhances the casing current amplitude by several factors, thereby improving signal strength and sensitivity of the measurement to the stimulated zone.

Next, we examine the impact of the surface electrode's location on the borehole EM measurements by moving it from (0, 1400 and 0 m) to (1400, 0 and 0 m) with the downhole electrode connected to the well at $z = 500$ m. Note that this moves the return electrode from a position roughly perpendicular to the trajectory of the deviated portion of the well, to a position that is laterally close to overlying the energized well casing. Figure 12 shows the borehole EM measurements in this configuration. Compared to Figure 9 where the surface electrode is grounded at (0, 1400 and 0 m), Figure 12 shows an overall decrease in sensitivity to the stimulated zones. For example, only one horizontal magnetic field component (i.e. B_x, Figure 12i) is sufficiently sensitive to the stimulated zone in this configuration. Furthermore, the sensitivity of the vertical electric field measurements (Figure 12l) is substantially reduced. The reduced sensitivity is due to the fact that with the surface electrode grounded near the observation well, the primary fields from the surface current source effectively mask the secondary fields from the stimulated zones. However, as the downhole electrode is moved downward from $z = 500$ m (Figure 12) to 1000 m (Figure 13), the energized injection well provides more current in and around the stimulated zone, overcoming the masking effects and improving the overall

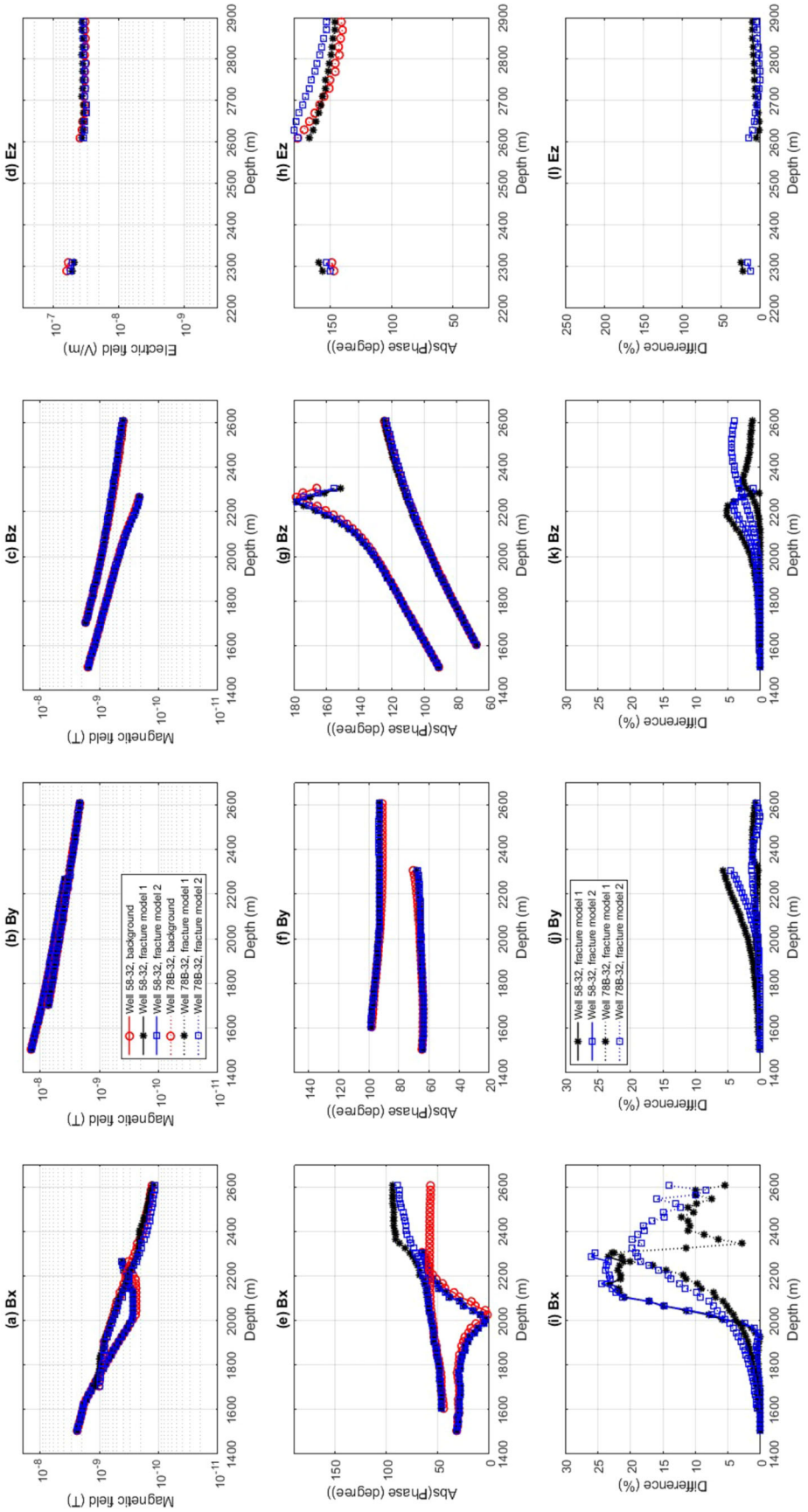

FIGURE 12 Comparison in simulated electromagnetic (EM) amplitude measurements (first row [a–d]) at 50 Hz before and after stimulation, the phase (second row [e–h]) and their relative amplitude differences (third row [i–k]). Three components of the magnetic fields (first to third column) and the vertical electric fields (fourth column) are plotted. The surface electrode is grounded at (1.4, 0 and 0 km), and the downhole electrode is connected to the inside of the casing at (0, 0 and 500 m).

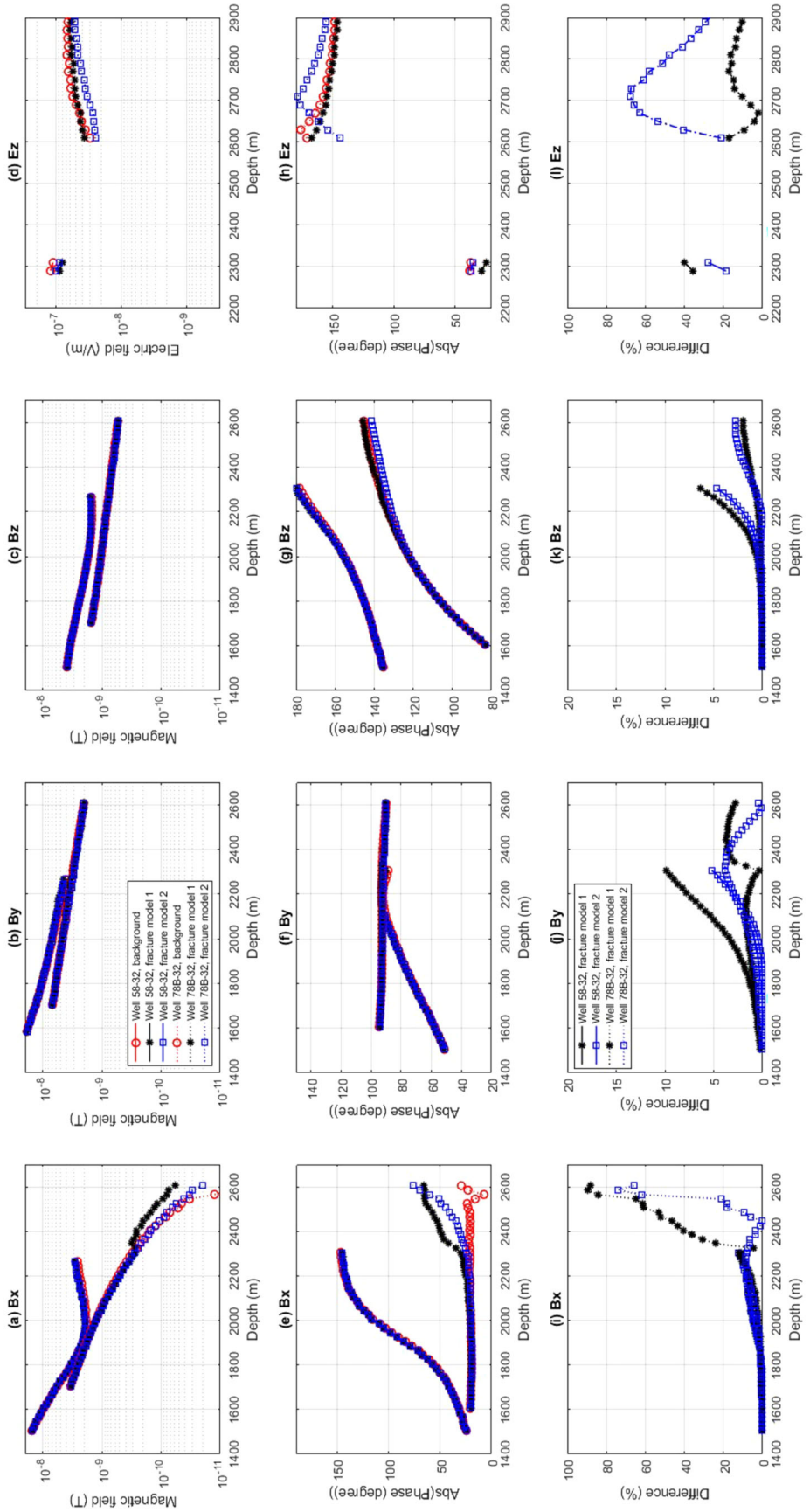

FIGURE 13 Comparison in simulated electromagnetic (EM) amplitude measurements (first row [a–d]) at 50 Hz before and after stimulation, the phase (second row [e–h]) and their relative amplitude differences (third row [i–l]). Three components of the magnetic fields (first to third column) and the vertical electric fields (fourth column) are plotted. The surface electrode is grounded at (1.4, 0 and 0 km), and the downhole electrode is connected to the inside of the casing at (0, 0 and 1 km).

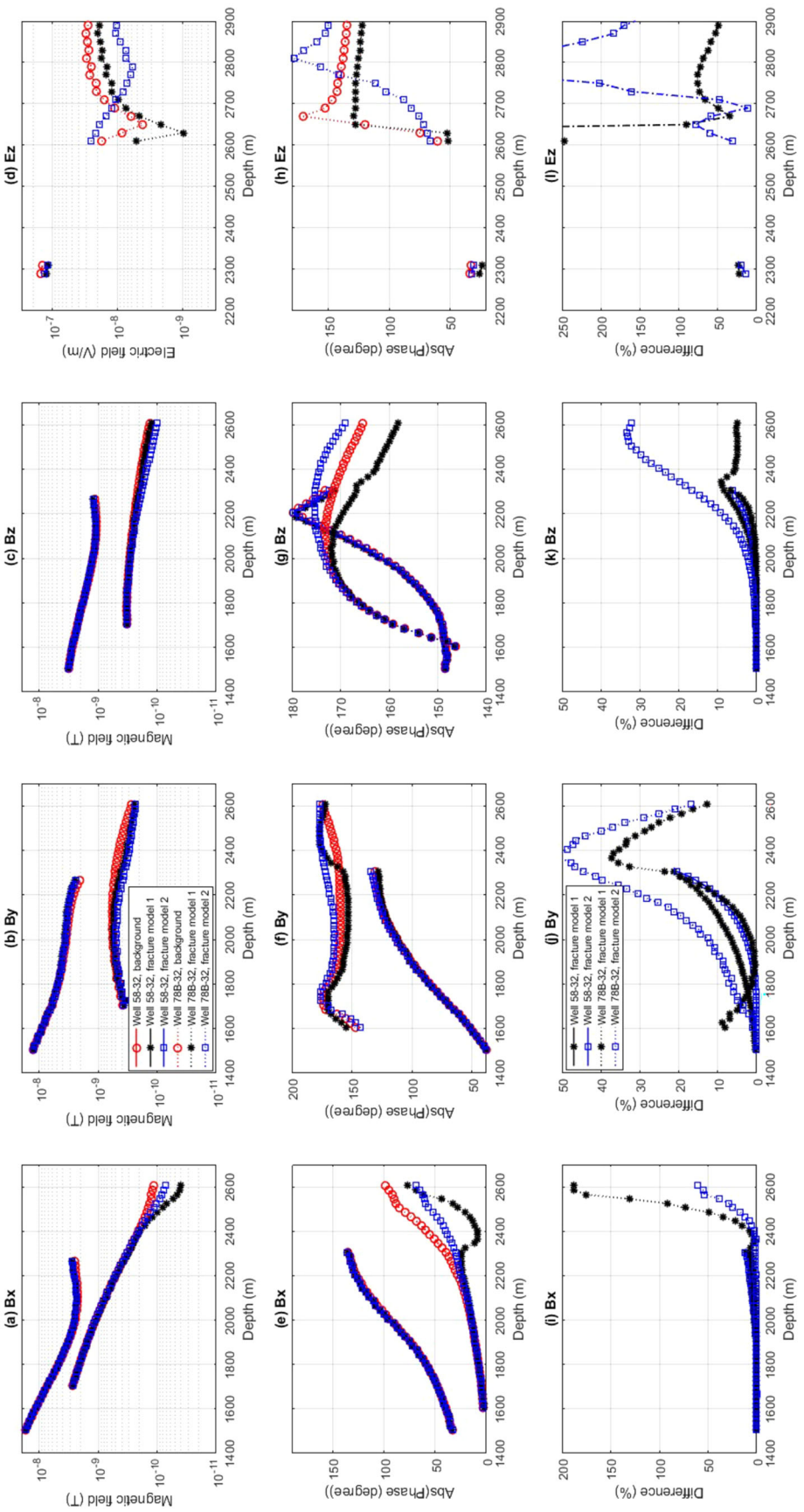

FIGURE 14 Comparison in simulated electromagnetic (EM) amplitude measurements (first row [a–d]) at 50 Hz before and after stimulation, the phase (second row [e–h]) and their relative amplitude differences (third row [i–l]). Three components of the magnetic fields (first to third column) and the vertical electric fields (fourth column) are plotted. The surface electrode is grounded at (−1.4, 0 and 0 km), and the downhole electrode is connected to the inside of the casing at (0, 0 and 1 km).

sensitivity to the stimulated zone. Nevertheless, these results (Figure 13) are much less effective in comparison to those (Figure 10) where the surface electrode is grounded away from both the injection and observation wells.

Last, we examine the borehole EM measurements when the surface electrode is grounded at (−1400, 0 and 0 m), another surface position sufficiently distant away from both the injection and observation wells. Figure 14 shows the resulting borehole EM measurements, which exhibit sufficiently large EM amplitudes and sensitivity to the stimulated zone, similar in amplitude but different in character from those obtained when the surface electrode is grounded at (0, 1400 and 0 m) in Figure 10. The resulting differences without much loss in sensitivity indicate that we can obtain additional data by grounding the surface electrode at various locations and repeating EM measurements. This approach can provide a more comprehensive dataset that enables us to better understand various aspects of the stimulated zone.

CONCLUSIONS

We have proposed and analysed a new electromagnetic (EM) data acquisition configuration for monitoring deep localized zones that are generated during stimulation to produce an engineered geothermal reservoir system at the Utah Frontier Observatory for Research in Geothermal Energy (FORGE) site. The depths of the stimulation at this site coupled with relatively small stimulation zone imply that conventional surface-based EM methods cannot provide sufficient sensitivity. The configuration simulated in this paper overcomes this by combining borehole EM measurements with an energized steel-casing source. To evaluate the sensitivity of this configuration, a task not fully attainable through existing analytical or numerical modelling solutions, the proposed workflow for simulating the energized steel casing uses a vertical equivalent of a deviated cased well, calculates casing current densities when embedded in a layered model derived from resistivity structures along the trajectory of the deviated well, replaces the current densities with a series of electric dipoles and then aligns the dipoles along the true trajectory of the well inside an original 3D resistivity model. In the geological context of the FORGE site, this workflow serves as a valuable first-order approximation tool for assessing the sensitivity of employing the energized casing source in conjunction with the vertical EM profiling system for detecting a deep, localized enhanced geothermal system at the FORGE site.

Our numerical modelling study shows that combined with the energized casing source, the borehole EM measurement system offers sufficiently large magnetic field amplitudes and sensitivity to the stimulated zones and can distinguish between the parallel-fracture anisotropic reservoir and the isotropic case, providing valuable insights into the fracture system of the stimulated zone at the FORGE site. The 3D modelling study also suggests that the vertical electric field measurements are highly sensitive to the stimulated zone and thus can be used as additional constraints for detecting and imaging the target. Additional monitoring data are provided by grounding the surface electrode at various locations and repeating borehole EM measurements. In this study, we have examined the detection sensitivity of the proposed EM configuration to the deep localized stimulated zone. Our forthcoming work will include 3D inverse modelling experiments to evaluate the imaging sensitivity of the proposed EM configuration to the stimulated zone. Based on these encouraging numerical modelling evaluation results, our current plans are to deploy the system and make a suite of measurements at the FORGE just before and after the stimulation. We hope that this work will serve as a useful guide and reference for planning, modelling and evaluating the proposed EM geophysical monitoring design for geothermal and geological sequestration applications.

ACKNOWLEDGEMENTS

The funding for this work was provided by the U.S. DOE EERE Geothermal Technologies Office to Utah FORGE and the University of Utah under Project DE-EE0007080 Enhanced Geothermal System Concept Testing and Development at the Milford City, Utah Frontier Observatory for Research in Geothermal Energy (Utah FORGE) site. The authors express their gratitude to Dr. Aleta Finnila of Golder for providing fracture modelling data and valuable comments. The authors extend their appreciation to Dr. Lindsey Heagy and the SimPEG development team at The University of British Columbia for their electromagnetic modelling codes, Dr. Mike Hoversten of LBNL for an effective medium modelling code and Dr. Andy McAliley of the US Geological Survey for the python version of the method of moment modelling code used for computing casing currents.

DATA AVAILABILITY STATEMENT

The modelling data presented in this research are available and can be obtained by contacting the corresponding author.

REFERENCES

Alumbaugh, D., Um, E., Wilt, W., Nichols, E. & Osato, K. (2023) Deep borehole EM deployment for fracture mapping at the FORGE geothermal site. In: *Proceedings of the 48th Workshop on Geothermal Reservoir Engineering, 2023, Stanford, California*. Stanford University.

Beskardes, G.D., Weiss, C.J., Um, E., Wilt, M. & MacLennan, K. (2021) The effects of well damage and completion designs on geoelectrical responses in mature wellbore environments. *Geophysics*, 86(6), E355–E366.

Berryman, J.G. & Hoversten, G.M. (2013) Modelling electrical conductivity for earth media with macroscopic fluid-filled fractures. *Geophysical Prospecting*, 61(2), 471–493.

Blackwell, D.D., Negraru, P.T. & Richards, M.C. (2006) Assessment of the enhanced geothermal system resource base of the United States. *Natural Resources Research*, 15, 283–308.

Boitnott, G.N. & Kirkpatrick, A. (1997) Interpretation of field seismic tomography at the Geysers geothermal field, California. In: *Proceedings of the 22nd Workshop on Geothermal Reservoir Engineering*. Stanford, Stanford University. pp. 391–398.

Breede, K., Dzebisashvili, K., Liu, X. & Falcone, G. (2013) A systematic review of enhanced (or engineered) geothermal systems: past, present and future. *Geothermal Energy*, 1, 1–27.

Börner, J.H., Bär, M. & Spitzer, K. (2015) Electromagnetic methods for exploration and monitoring of enhanced geothermal systems–a virtual experiment. *Geothermics*, 55, 78–87.

Castillo-Reyes, O., Queralt, P., Marcuello, A. & Ledo, J. (2021) Land CSEM simulations and experimental test using metallic casing in a geothermal exploration context: Vallès basin (NE Spain) case study. *IEEE Transactions on Geoscience and Remote Sensing*, 60, 1–13.

Commer, M., Hoversten, G.M., & Um, E.S. (2015) Transient-electromagnetic finite-difference time-domain earth modeling over steel infrastructure. *Geophysics*, 80(2), E147–E162.

Cuevas, N.H. (2014) Analytical solutions of EM fields due to a dipolar source inside an infinite casing. *Geophysics*, 79(5), E231–E241.

Cuevas, N.H. (2019) Surface-borehole electromagnetic method-a review on the technology development and potential for geothermal applications. In: *EAGE/BVG/FKPE joint workshop on borehole geophysics and geothermal energy, 2019*. Bunnik, The Netherlands, European Association of Geoscientists & Engineers. pp. 1–2.

Dobson, P., Dwivedi, D., Millstein, D., Krishnaswamy, N., Garcia, J. & Kiran, M. (2020) Analysis of curtailment at The Geysers geothermal field, California. *Geothermics*, 87, 101871.

Dyer, B.C., Schanz, U., Ladner, F., Haring, M.O. & Spillman, T. (2008) Microseismic imaging of a geothermal reservoir stimulation. *The Leading Edge*, 27(7), 856–869.

Finnila, A. & Podgorney, R. (2020) Exploring hydraulic fracture stimulation patterns in the forge reservoir using multiple stochastic DFN realizations and variable stress conditions. In: *Proceedings of the 45th Workshop on Geothermal Reservoir Engineering*. Stanford, CA, Stanford University.

Gao, G., Alumbaugh, D., Zhang, P., Liu, J., Zhang, H., Levesque, C., Rosthal, R., Abubakar, A. & Habashy, T. (2008) Practical implications of nonlinear inversion for cross-well electromagnetic data collected in cased-wells. In: *78Th annual international meeting, SEG annual meeting*. Houston, SEG. pp. 299–303.

Gritto, R. & Jarpe, S.P. (2014) Temporal variations of Vp/Vs-ratio at The Geysers geothermal field, USA. *Geothermics*, 52, 112–119.

Gritto, R., Jarpe, S.P. & Alumbaugh, D.L. (2022) New large-scale passive seismic monitoring at The Geysers geothermal reservoir, CA, USA. In: *Proceedings, 47th Workshop on Geothermal Reservoir Engineering*. Stanford, CA, Stanford University.

Heagy, L.J., Cockett, R., Kang, S., Rosenkjaer, G.K. & Oldenburg, D.W. (2017) A framework for simulation and inversion in electromagnetics. *Computers & Geosciences*, 107, 1–19.

Heagy, L.J. & Oldenburg, D.W. (2019) Modeling electromagnetics on cylindrical meshes with applications to steel-cased wells. *Computers & Geosciences*, 125, 115–130.

Hoversten, G.M., Commer, M., Haber, E. & Schwarzbach, C. (2015), Hydro-frac monitoring using ground time-domain electromagnetic. *Geophysical Prospecting*, 63, 1508–1526.

Johnston, R. & Shrallow, J. (2011) Ambiguity in microseismic monitoring. In: 81st annual international meeting Society of Exploration Geophysicists, expanded abstracts. Houston, Society of Exploration Geophysicists. pp. 1514–1518.

Kneafsey, T.J., Dobson, P., Blankenship, D., Morris, J., Knox, H., Schwering, P. et al. (2018) An overview of the EGS collab project: field validation of coupled process modeling of fracturing and fluid flow at the Sanford Underground Research Facility, Lead, SD. In: *43Rd Workshop on Geothermal Reservoir Engineering*. Stanford, CA, Stanford University.

Kohnke, C., Liu, L., Streich, R. & Swidinsky, A. (2018) A method of moments approach to model the electromagnetic response of multiple steel casings in a layered earth. *Geophysics*, 83(2), WB81–WB96.

Kolditz, O., Bauer, S., Bilke, L., Böttcher, N., Delfs, J.O., Fischer, T. et al. (2012) OpenGeoSys: an open-source initiative for numerical simulation of thermo-hydro-mechanical/chemical (THM/C) processes in porous media. *Environmental Earth Sciences*, 67, 589–599.

Kordy, M., Wannamaker, P., Maris, V., Cherkaev, E. & Hill, G. (2016) 3-D magnetotelluric inversion including topography using deformed hexahedral edge finite elements and direct solvers parallelized on SMP computers–part I: forward problem and parameter Jacobians. *Geophysical Journal International*, 204(1), 74–93.

Lellouch, A., Lindsey, N.J., Ellsworth, W.L. & Biondi, B.L. (2020) Comparison between distributed acoustic sensing and geophones: downhole microseismic monitoring of the FORGE geothermal experiment. *Seismological Society of America*, 91(6), 3256–3268.

Lin, G. & Wu, B. (2018) Seismic velocity structure and characteristics of induced seismicity at The Geysers geothermal field, eastern California. *Geothermics*, 71, 225–233.

Lindsey, N.J., Kaven, J.O., Davatzes, N. & Newman, G.A. (2016) Compartmentalization of the Coso East Flank geothermal field imaged by 3-D full-tensor MT inversion. *Geophysical Journal International*, 208(2), 652–662.

Lu, S.M. (2018) A global review of enhanced geothermal system (EGS). *Renewable and Sustainable Energy Reviews*, 81, 2902–2921.

Marsala, A.F., Hibbs, A.D. & Morrison, H.F. (2014) Borehole casing sources for electromagnetic imaging of deep formations. In: *SPE annual technical conference and exhibition*. Calgary, SPE, pp. SPE–170845

Miura, Y., Osato, K., Takasugi, S., Muraoka, H. & Yasukawa, K. (1996) Development of the vertical electro magnetic profiling (VEMP) method. *Journal of applied Geophysics*, 35(2–3), 191–197.

Moore, J., McLennan, J., Allis, R., Pankow, K., Simmons, S., Podgorney, R. et al. (2019) The Utah Frontier Observatory for Research in Geothermal Energy (FORGE): an international laboratory for enhanced geothermal system technology development. In: *Proceedings 44th Workshop on Geothermal Reservoir Engineering*. Stanford, CA, Stanford University. pp. 11–13.

Moore, J., McLennan, J., Pankow, K., Simmons, S., Podgorney, R., Wannamaker, P. et al. (2020) The Utah Frontier Observatory for Research in Geothermal Energy (Forge): a laboratory for characterizing, creating and sustaining enhanced geothermal systems. In: *Proceedings of the 45th Workshop on Geothermal Reservoir Engineering*. Stanford, CA, Stanford University.

Moos, D. & Zoback, M.D. (1983) In situ studies of velocity in fractured crystalline rocks. *Journal of Geophysical Research: Solid Earth*, 88(B3), 2345–2358.

Muñoz, G. (2014) Exploring for geothermal resources with electromagnetic methods. *Surveys in Geophysics*, 35, 101–122.

Newman, G.A., Gasperikova, E., Hoversten, G.M. & Wannamaker, P.E. (2008) Three-dimensional magnetotelluric characterization of the Coso geothermal field. *Geothermics*, 37(4), 369–399.

Orujov, G., Swidinsky, A. & Streich, R. (2022) Do metal infrastructure effects cancel out in time-lapse electromagnetic measurements? *Geophysics*, 87(2), E91–E101.

Oye, V., Langet, N., Hasting, M., Lecomte, I., Messeiller, M. & Reid, P. (2012) Microseismic monitoring of the hydraulic stimulation at the Paralana enhanced geothermal system, South Australia. *First Break*, 30(7), 91–95.

Peacock, J., Thiel, S., Reid, P. & Heinson, G. (2012) Magnetotelluric monitoring of a fluid injection: example from an enhanced geothermal system. *Geophysical Research Letters*, 39(18), L18403.

Peacock, J., Thiel, S., Heinson, G. & Reid, P. (2013) Time-lapse magnetotelluric monitoring of an enhanced geothermal system. *Geophysics*, 78(3), B121–B130.

Peacock, J., Earney, T., Mangan, M., Schermerhorn, W., Glen, J., Walters, M. et al. (2020) Geophysical characterization of the Northwest Geysers geothermal field, California. *Journal of Volcanology and Geothermal Research*, 399, 106882.

Peacock, J., Alumbaugh, D., Mitchell, M. & Hartline, C. (2022) Repeat magnetotelluric measurements to monitor the Geysers steam field in Northern California. In: *47Th Workshop on Geothermal Reservoir Engineering*. Stanford, California, Stanford University.

Schlumberger. (2005) *Schlumberger log interpretation charts*. Houston, TX: Schlumberger.

Tang, W., Li, Y., Swidinsky, A. & Liu, J. (2015) Three-dimensional controlled-source electromagnetic modelling with a well casing as a grounded source: a hybrid method of moments and finite element scheme. *Geophysical Prospecting*, 63, 1491–1507.

Tester, J., Anderson, B., Batchelor, A., Blackwell, D., DiPippo, R., Drake, E. et al. (2006) The future of geothermal energy. Cambridge, MA: Massachusetts Institute of Technology.

Um, E.S., Commer, M., Newman, G.A., & Hoversten, G.M. (2015) Finite element modelling of transient electromagnetic fields near steel-cased wells. *Geophysical Journal International*, 202(2), 901–913.

Um, E., Kim, J. & Wilt, M. (2020) 3D borehole-to-surface and surface electromagnetic modeling and inversion in the presence of steel infrastructure. *Geophysics*, 85(5), 139–E152.

Wannamaker, P., Rose, P., Doerner, W., Berard, B., McCulloch, J. & Nurse, K. (2004) Magnetotelluric surveying and monitoring at the Coso geothermal area, California, in support of the enhanced geothermal systems concept: survey parameters and initial results. In: *29Th Workshop on Geothermal Reservoir Engineering, Stanford, California*. Stanford University, pp. 287–294.

Wannamaker, P., Simmons, S., Miller, J., Hardwick, C., Erickson, B., Bowman, S. et al. (2020) Geophysical activities over the Utah FORGE site at the outset of project phase 3. In: *Proceedings, 45th Workshop on Geothermal Reservoir Engineering*. Stanford, CA: Stanford University, pp. 1–14.

Weiss, C.J. (2017) Finite-element analysis for model parameters distributed on a hierarchy of geometric simplices. *Geophysics*, 82(4), E155–E167.

Wilt, M., Takasugi, S., Uchida, T., Kasameyer, P., Lee, K. & Lippmann, M. (1997) Fracture mapping in geothermal fields with long-offset induction logging. In: *Proceedings: twenty-second Workshop on Geothermal Reservoir Engineering*. Stanford, CA, Stanford University, pp. 2–3 to 2–6.

Wilt, M., Mallan, R., Kasameyer, P. & Kirkendall, B. (2002) 3D extended logging for geothermal resources: field trials with the Geo-BILT system. In: 27Th *Workshop on Geothermal Reservoir Engineering*. Stanford, CA, Stanford University, pp. 23–25.

Wu, X. & Habashy, T.M. (1994) Influence of steel casings on electromagnetic signals. *Geophysics*, 59(3), 378–390.

Xing, P., Damjanac, B., Radakovic-Guzina, Z., Torres, M., Finnila, A., Podgorney, R. et al. (2022) Numerical simulation of stimulations at The Utah FORGE site using the designed pumping schedules. In: *Proceedings of the Geothermal Rising conference*. Davis, CA, Geothermal Rising. pp. 618–628.

How to cite this article: Um, E.S., Alumbaugh, D., Capriotti, J., Wilt, M., Nichols, E., Li, Y. et al. (2024) 3D modeling of deep borehole electromagnetic measurements with energized casing source for fracture mapping at the Utah Frontier Observatory for Research in Geothermal Energy. *Geophysical Prospecting*, 1–25.
https://doi.org/10.1111/1365-2478.13579

APPENDIX 1
COMPARISON OF CASING CURRENTS BETWEEN DEVIATED WELL AND ITS VERTICALIZED COUNTERPART USING HIERARCHICAL MODELLING METHOD

Weiss (2017) described a hierarchical method of modelling infinitely thin elements of conductivity in a finite-element discretization of Maxwell's equations. These either exist along faces in the mesh for plate-like elements or along edges of the mesh for linear elements. The methodology also naturally extends to finite volume discretization in the SimPEG framework. Linear conductive elements, such as the wells of interest in this study, are represented by infinitely thin cells at mesh edges along the well path.

We express the finite volume form of Maxwell's equations from Heagy et al. (2017), solving for the electric field defined along edges of the mesh:

$$\left(C^T M_{f\mu^{-1}} C + i\omega M_{e\sigma}\right) e = -i\omega s_e, \qquad \text{(A1)}$$

where C is the discretized curl operator going from edges to faces, $M_{f\mu^{-1}}$ is a face inner product matrix with respect to the inverse of permeability, $M_{e\sigma}$ is an edge inner product matrix with respect to the conductivity, s_e is the integrated source term, ω is the source's angular frequency, and e is the electric field defined along edges.

The hierarchical method adds additional cells with no volume to account for infinitely small features in the finite volume method. According to Weiss (2017), this discretization assumes that the electric field is parallel to the element, and that within the element, the magnetic field is constant, which is valid for our highly conductive well. These assumptions leave only the second term on the left-hand side of Equation (A1) accounting for the integral of the electric field itself. The finite volume inner product integral over these edge elements is then defined as

$$\langle u_i,\ v_i \rangle\ = \int_{V_i} u_i \kappa_i v_i\ d\ l_i, \tag{A2}$$

$$\kappa_i\ =\ \sigma_i A_i,$$

where σ_i is the conductivity of the edge element, and A_i is the physical cross-sectional area of the feature it represents (u_i and v_i are the standard finite volume test functions defined on edge i). Essentially these parameters correspond to integrating the electric field over the cross section of the well and representing that value along the linear element. This results in another diagonal mass matrix added to the discretized forms of the electric fields:

$$\left(C^T M_{f\,\mu^{-1}} C + i\omega(M_{e\sigma} + M_{e\kappa})\right) e\ =\ -i\omega s_e. \tag{A3}$$

Because this form is independent of the mesh, we can use a mesh that directly discretizes the well path along its edges. This would require either a tetrahedral or a curvilinear mesh for deviated wells. For the comparison between the equivalent current source density of a deviated well and the currents derived from the hierarchical method, we used a curvilinear mesh. The workflow to obtain currents along the well path is then simply to extract the electric field along the well-path edges and multiply by κ.

A comparison of currents calculated from the two methods is shown in Figure A1.1. For consistency, we employ the same well trajectory as depicted in Figure 5, labelled 16A(78)-32. The downhole electrode is grounded at a depth of 1 km, whereas the surface electrode is grounded 1400 m away from the wellhead. We use the same casing geometry and properties described in the main text. The source frequency is set to 0.25 Hz. For simplicity, the background model is a homogeneous half-space with a resistivity of 100 Ω m. As shown in A1.1, for most of the well path, we see less than 3% difference. It then increases to greater than a 5% difference for the last 200 m of the well. Overall, the two solutions show good agreement, supporting the numerical modelling experiments presented in the main text.

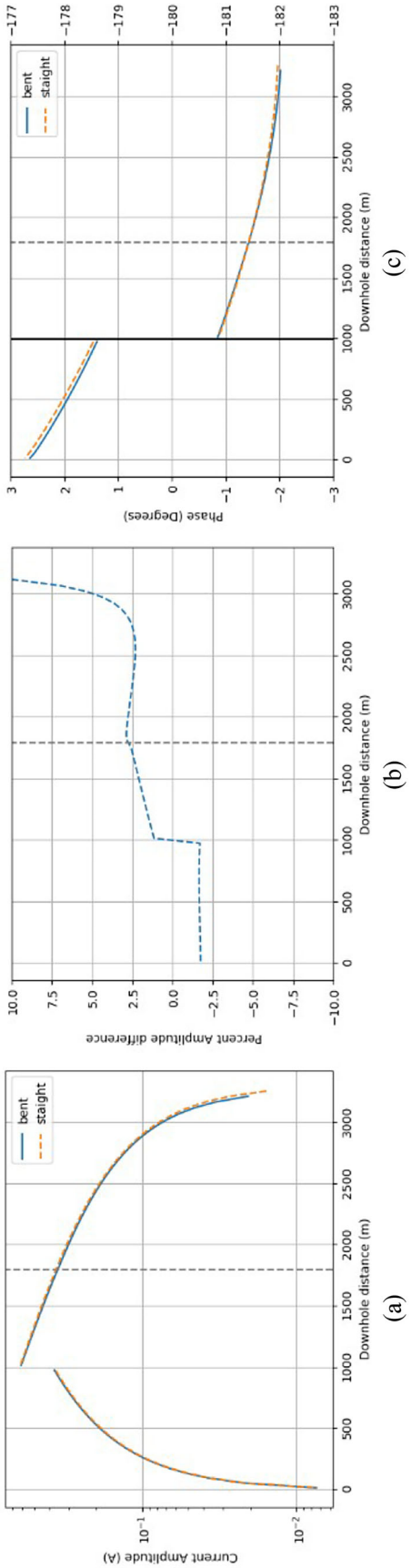

FIGURE A1.1 Comparison of currents calculated from the deviated well and its corresponding verticalized well. Bent and straight indicate the casing current along the deviated well (i.e. the hierarchical modelling solution) and the casing current along the verticalized well (i.e. the 3D SimPEG solutions using the cylindrical coordinate system), respectively. (a) The current amplitude plots. (b) The amplitude difference (%) plots. (c) The phase (degree) plots.

APPENDIX 2
EFFECTS OF MAGNETIC PERMEABILITY OF ENERGIZED CASING SOURCE ON BOREHOLE EM MEASUREMENTS

As far as the authors are aware, the effects of magnetic permeability of energized casing sources on borehole EM data have not been previously investigated. Research on incorporating the magnetic permeability of casing into 3D EM modelling and inversion in a computationally efficient manner is also still in its early stages. In this appendix, using a 2D EM modelling code, we briefly examine the effects of magnetic permeability of energized casing sources on borehole EM data and present two potential techniques for addressing these effects without directly modelling the permeability.

The effects of steel casing's magnetic permeability depend on source frequency. At DC or low frequencies, they are often disregarded. However, as the frequency increases, they become significant and cannot be ignored. To examine the effects of magnetic permeability of energized steel casing on borehole EM measurements, we simulate both magnetically permeable ($\mu_r = 100$) and non-permeable ($\mu_r = 1$) cased source well at 50 Hz using the 2D SimPEG code (Heagy & Oldenburg, 2019). We use a 3300 m deep vertical cased well of which the diameter and wall thickness are the same as those used in the main text. One electrode is connected to the inside of the well casing at 1000 m in depth and the other to the wellhead. Note that instead of being grounded on the surface away from the wellhead, the return electrode is connected to the wellhead because the 2D modelling code requires the source to be positioned along the axis of the well. A vertical observation well is located 200 m distant from the source well. The FORGE's layered resistivity structures (Figure 7) are used as the background model for Figure A2.1.

Figure A2.1 shows the borehole EM measurements (E_z and B_x) obtained from both magnetically permeable and non-permeable source wells, demonstrating that the magnetic permeability has a significant effect on both electric and magnetic fields. First, we note that the magnetically permeable casing does not strongly change the shapes of the EM measurements but rather shifts them in amplitude and phase. Thus, we see the possibility of removing these effects by multiplying the EM fields by a complex parameter that scales the amplitude of the EM fields and adjusts their phases. This approach is similar to that used in removing the casing effect in crosswell EM data processing (Gao et al., 2008). Figure A2.1 shows that the EM responses from the magnetically permeable casing source reasonably agree with those from the non-permeable well after multiplication by a complex scaling parameter. In order to implement and evaluate this approach, EM inverse modelling algorithms need to be modified to enable the estimation of not only electrical conductivity parameters but also scaling parameters.

Another possible approach for mitigating the effects of casing's magnetic permeability on borehole EM data is to use the ratio of borehole EM fields. Figure A2.2 shows that the magnetically permeable casing source causes a shift in both horizontal electric and magnetic fields (e.g. E_x and B_x). Based on the observation, we think that it would be possible to interpret borehole EM data without explicitly modelling the casing's magnetic permeability by utilizing the ratio of the electric field (E_x) to the magnetic field (B_x). To demonstrate, we inserted a 300 m thick disk-shaped fractured zone with a radius of 150 m below the casing source. The resistivity of the fractured zone was set to 270 Ω m, which is similar to the resistivity of fracture model 2 used in the main text. Figure A2.2a,b shows the EM fields with and without the fractured zone, considering both permeable and non-permeable casing source wells. It should be noted that the magnetically permeable casing distorts both E_x and B_x in a very similar manner. Therefore, the ratio plot of E_x to B_x for the permeable casing source is insensitive to its magnetic permeability and agrees with that of the non-permeable one as shown in Figure A2.2c. In order to implement and evaluate this second approach, EM inverse modelling algorithms need to be modified accordingly. It is also essential to reliably measure horizontal EM fields in a borehole environment, which is often considered more challenging compared to measuring their vertical components.

In this appendix, we have demonstrated the impact of the magnetically permeable casing source on borehole EM data and proposed the two potential techniques for removing these effects from the borehole EM data. However, although Figures A2.1 and A2.2 demonstrate good agreement in the simple modelling scenarios presented here, we anticipate that there could be other casing EM modelling scenarios where the techniques showcased here may not be effective. To gain a comprehensive understanding of the impact of casing's magnetic permeability on casing source EM, further modelling experiments and analysis are required. We also anticipate that the application of these approaches to real field data would remain challenging due to a different magnetic permeability value at each casing segment, as well as its dependence on temperature and its change over time in EGS environments. We also expect that measuring horizontal EM fields inside an observation well is more vulnerable to noises than measuring the vertical fields. 3D forward and inverse modelling algorithms will also need to be modified to incorporate the proposed approaches discussed here. Therefore, further research on this topic is necessary to ensure reliable data interpretation. We think that such research will be critical for the advancement of reliable interpretation of borehole EM data in the use of magnetically permeable casing sources.

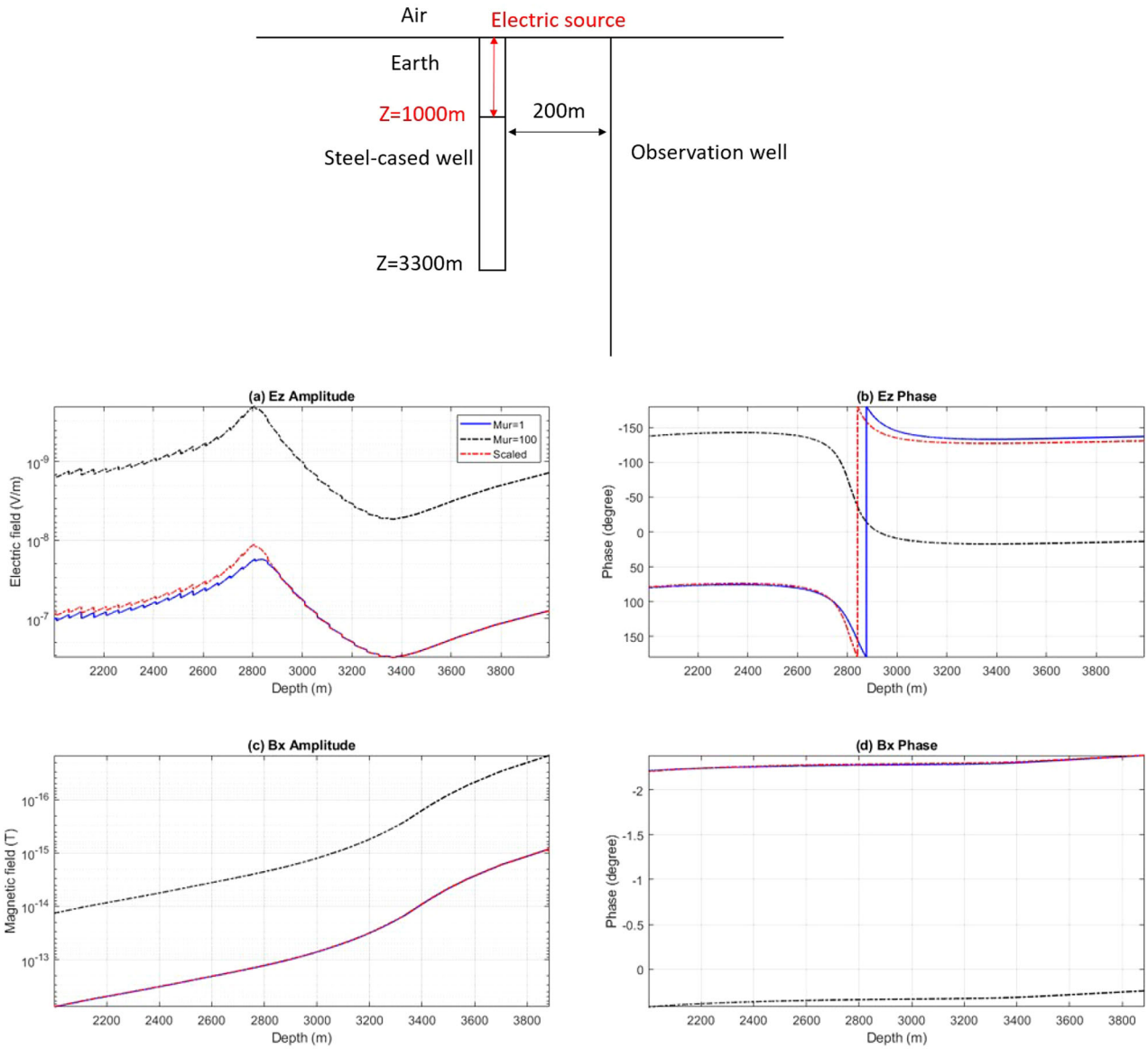

FIGURE A2.1 Comparison of borehole electromagnetic (EM) measurements between magnetically permeable ($\mu_r = 100$) and non-permeable ($\mu_r = 1$) steel casing sources. The top shows a simple casing source EM model used here. The EM measurements resulting from the magnetically permeable cased source, which are multiplied by a complex scaling parameter, are denoted in red.

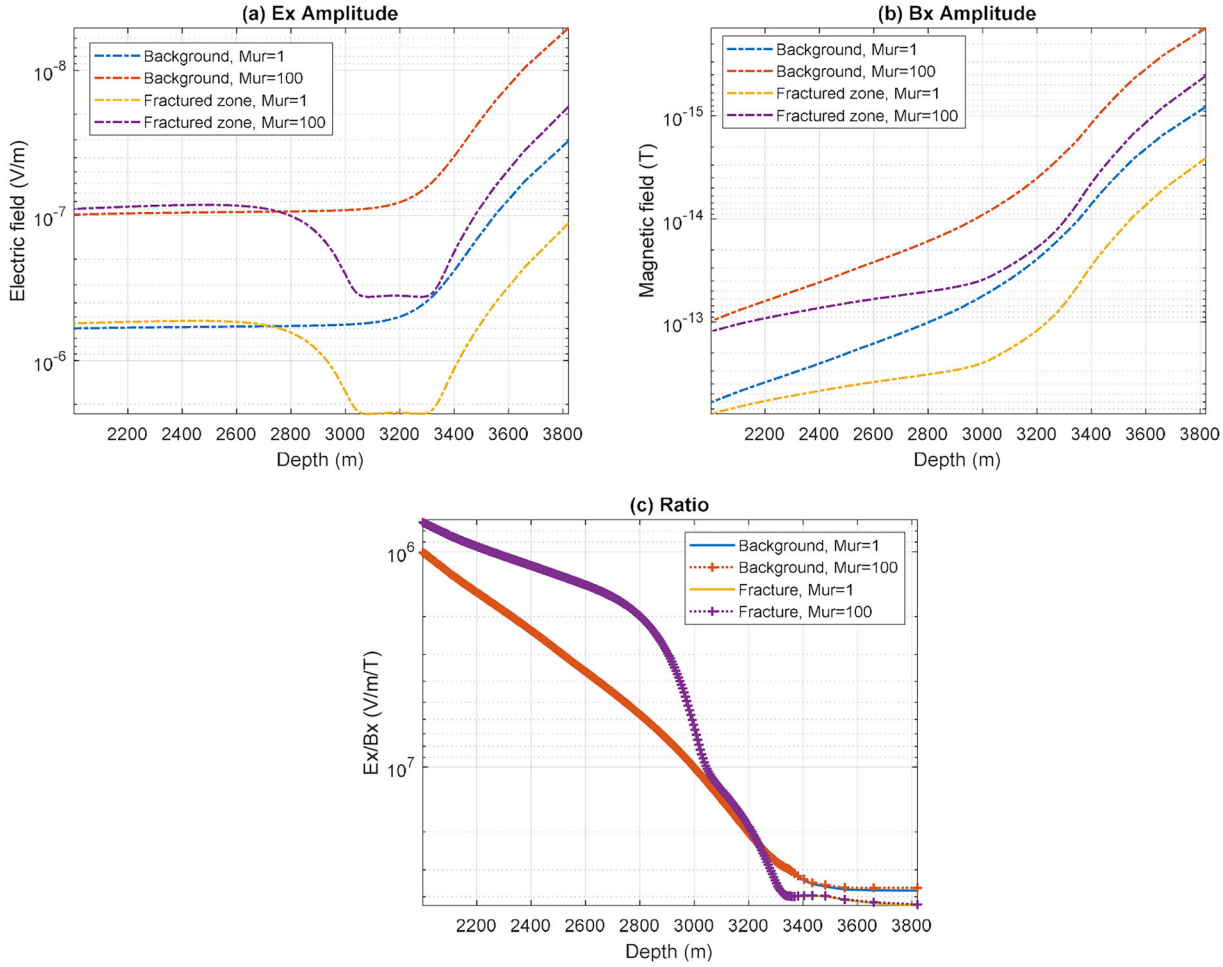

FIGURE A2.2 Comparison of borehole electromagnetic (EM) measurements with and without the conductive fractured zone between magnetically permeable ($\mu_r = 100$) and non-permeable ($\mu_r = 1$) steel casing sources and their ratios.